

Award Number: W81XWH-11-2-0076

TITLE: New Methods of Low-Field Magnetic Resonance Imaging for Application to Traumatic Brain Injury

PRINCIPAL INVESTIGATOR: Matthew S. Rosen, Ph.D.

CONTRACTING ORGANIZATION: Harvard University, Cambridge MA 02138

REPORT DATE: February 2015

TYPE OF REPORT: Annual

PREPARED FOR: U.S. Army Medical Research and Materiel Command
Fort Detrick, MD 21702-5012

DISTRIBUTION STATEMENT:

Approved for public release; distribution unlimited

The views, opinions and/or findings contained in this report are those of the author(s) and should not be construed as an official Department of the Army position, policy or decision unless so designated by other documentation.

REPORT DOCUMENTATION PAGE

*Form Approved
OMB No. 0704-0188*

Public reporting burden for this collection of information is estimated to average 1 hour per response, including the time for reviewing instructions, searching existing data sources, gathering and maintaining the data needed, and completing and reviewing this collection of information. Send comments regarding this burden estimate or any other aspect of this collection of information, including suggestions for reducing this burden to Department of Defense, Washington Headquarters Services, Directorate for Information Operations and Reports (0704-0188), 1215 Jefferson Davis Highway, Suite 1204, Arlington, VA 22202-4302. Respondents should be aware that notwithstanding any other provision of law, no person shall be subject to any penalty for failing to comply with a collection of information if it does not display a currently valid OMB control number. **PLEASE DO NOT RETURN YOUR FORM TO THE ABOVE ADDRESS.**

1. REPORT DATE (DD-MM-YYYY) February 2015			2. REPORT TYPE Annual		3. DATES COVERED (From - To) 10 Jan 2014 - 9 Jan 2015	
4. TITLE AND SUBTITLE New Methods of Low-Field Magnetic Resonance Imaging for Application to Traumatic Brain Injury			5a. CONTRACT NUMBER			
			5b. GRANT NUMBER W81XWH-11-2-0076			
			5c. PROGRAM ELEMENT NUMBER			
6. AUTHOR(S) Matthew S. Rosen, PhD email: mrosen@cfa.harvard.edu			5d. PROJECT NUMBER			
			5e. TASK NUMBER			
			5f. WORK UNIT NUMBER			
7. PERFORMING ORGANIZATION NAME(S) AND ADDRESS(ES) Harvard University, Cambridge MA 02138			8. PERFORMING ORGANIZATION REPORT NUMBER			
9. SPONSORING / MONITORING AGENCY NAME(S) AND ADDRESS(ES) U.S. Army Medical Research and Materiel Command Fort Detrick, MD 21702-5012			10. SPONSOR/MONITOR'S ACRONYM(S)			
			11. SPONSOR/MONITOR'S REPORT NUMBER(S)			
12. DISTRIBUTION / AVAILABILITY STATEMENT Approved for public release; distribution unlimited.						
13. SUPPLEMENTARY NOTES						
14. ABSTRACT We are developing robust low-magnetic-field implementations of MRI (LFI) focused on brain imaging with two complimentary test scanner systems: electromagnet and permanent magnet based. We have also developing injury-sensitive MRI based on the detection of free radicals associated with injury using the Overhauser effect and subsequently imaging that modified nuclear polarization using low-field MRI (OMRI). We have been optimizing imaging sequences, image reconstruction, and parallel imaging based acceleration in this unique regime. Results include demonstration of an optimized head coil for 3D human brain imaging in the electromagnet LFI at 6.5 mT, preliminary 3D imaging in a 100 lb scanner based on a rotating permanent magnet array, and improved free-radical OMRI both <i>in vitro</i> and <i>in vivo</i> . Application of the suite of techniques and technologies from our work could advise future development of a deployable device with a high diagnostic impact, transforming diagnosis and monitoring of secondary injury prevalent in TBI.						
15. SUBJECT TERMS Low-field brain MRI, Injury-sensitive MRI, Free radical Overhauser imaging.						
16. SECURITY CLASSIFICATION OF:			17. LIMITATION OF ABSTRACT	18. NUMBER OF PAGES	19a. NAME OF RESPONSIBLE PERSON USAMRMC	
a. REPORT U	b. ABSTRACT U	c. THIS PAGE U	UU	48	19b. TELEPHONE NUMBER (include area code)	

Table of Contents

INTRODUCTION:	4
BODY:	5
Low Field Imagers (LFIs)	5
TASK 1A: Low-field MRI Hardware Development	5
<i>HALBACH ARRAY (PERMANENT MAGNET) LFI</i>	6
<i>EXTENSION TO 3D ENCODING</i>	7
<i>HIGH-EFFICIENCY HELMET DETECTORS FOR THE ELECTROMAGNET LFI</i>	14
<i>RECEIVE COIL DEVELOPMENT</i>	14
OMRI Injury Imaging	16
TASK 2A: OMRI Hardware Development	16
<i>IMPROVING RADICAL DETECTION SENSITIVITY THROUGH DOUBLE RESONATOR DESIGN</i>	17
KEY RESEARCH ACCOMPLISHMENTS:	20
REPORTABLE OUTCOMES:	21
CONCLUSION:	24
REFERENCES:	26
APPENDICIES:	28
<i>YEAR 4 STATEMENT OF WORK</i>	29
<i>ABSTRACTS ACCEPTED FOR PRESENTATION</i>	30
<i>MANUSCRIPTS PUBLISHED/ACCEPTED FOR PUBLICATION</i>	37

INTRODUCTION:

Year Four of this applied research program continues to build on advances by our collaboration in the development of novel methods and advanced hardware for low-magnetic-field MRI. Without major innovation, high-field MRI instruments offer limited utility for imaging TBI in widely deployable contexts. We focus our research effort on the high-risk and critical challenges that must be solved to enable deployment of a transportable human-head MRI system applicable to TBI imaging in battlefield medical facilities. Our goal is to establish proof-of-principle of a suite of techniques and technologies to advise future development of a field-deployable device with high diagnostic impact. This research effort has two specific aims:

Specific Aim 1: Develop a low-field human-head MRI system (LFI) suitable for high-resolution multi-nuclear imaging, and improve the ability to attain brain images based on the intrinsic *in vivo* ^1H NMR signal in this scanner.

This includes the development of *two* robust low-field scanner hardware methodologies (electromagnet based and permanent magnet based), the development of novel high-speed parallel imaging detection systems, and work on advanced adaptive reconstruction methods including navigators and sparse sampling.

Specific Aim 2: Develop injury-sensitive MRI based on converting the electron spin of free radicals associated with injury (specifically TBI) into nuclear polarization using the Overhauser effect and subsequently imaging that modified nuclear polarization using low-field MRI (**OMRI**). Successful demonstration of OMRI of free radicals associated with injury will be directly applicable to the MRI systems of **Aim 1**, enhancing image-based injury specificity and/or shortening scan acquisition time.

The development of this new MRI contrast mechanism may provide an unambiguous non-invasive *in vivo* marker for cerebral injury, and has potential for assisting the imaging of TBI at both low and high magnetic fields.

BODY:

Image quality in the 6.5 mT electromagnet LFI (Aim 1) continues to improve as our suite of hardware and image acquisition strategies matures. Validation of image quality in head-shaped phantoms continues, including images acquired using a new single-channel receiver coil optimized for human heads. This receiver coil design demonstrates performance exceeding that of the more complex multi-channel designs described previously. We report details of this design, as well as images acquired in a new multi-compartment head-shaped phantom developed for this work.

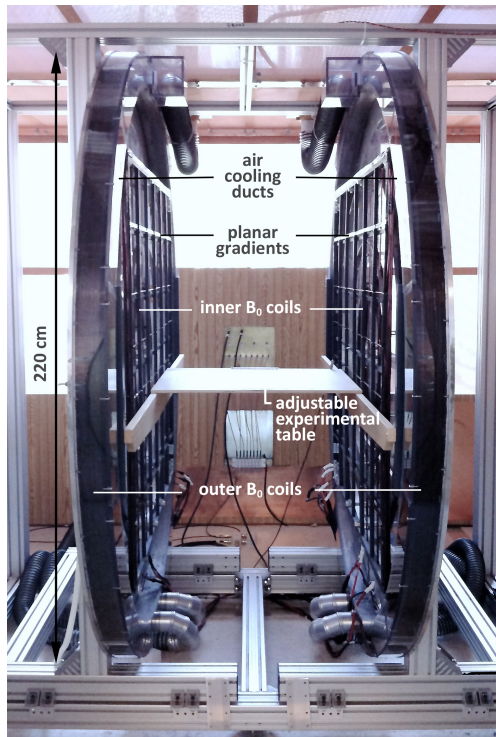
Additionally, we continue to make significant progress in our permanent magnet Halbach LFI experiment (Aim 1) toward the acquisition of true 3D datasets in the Halbach magnet portable imaging prototype [1]. For the first time, three key ingredients – “built-in” 2D encoding using a rotating B_0 encoding field, phase encoding with a linear phase RF transmit coil, and broadband RF pulses – were brought together to enable three-axis encoding in an inhomogeneous B_0 field with no gradient coils.

Our previous work on the detection of free radicals (Aim 2) focused on decreasing the image acquisition time in Overhauser MRI and on improving the detection limit to low concentrations of free radicals in synthetic radical solutions. Work on this task continues in collaboration with Professor of Chemistry D. Whitney King (Colby College. Dr. King’s laboratory has developed a portable calibrated superoxide generator, and will allow us to directly investigate OMRI sensitivity to biologically relevant superoxide at nanomolar to micromolar concentrations. This is a critical step to understand the biological relevance and applicability of the new method of free radical imaging developed under this grant. We determined that significant improvements were still needed in the manner in which our OMRI detection is performed before we could attain sensitivity to superoxide, and to that end have improved our OMRI detector hardware and attained a 3-fold improvement in SNR and, critically, wide-range tunability has been attained.

Low Field Imagers (LFIs)

TASK 1A: Low-field MRI Hardware Development

We continue to optimize hardware development for the human head LFI test bed systems (Aim 1) and for the OMRI system (Aim 2).



The 6.5 mT electromagnet LFI

The electromagnet LFI (shown below) is an ideal state-of-the art test bed for all of the novel acquisition, detection methodologies, and reconstruction algorithms including navigators and sparse sampling, and additionally will provide necessary experience and data to advise optimal construction and magnetic field for any future electromagnet-based deployable systems. Currently, this state-of-the-art scanner enables high-performance spectroscopy and 8-channel imaging at 6.5 mT, and is fully equipped for Overhauser DNP experiments.

The permanent magnet system is a lightweight (45 kg) and portable Halbach array. This Halbach array scanner is a highly specialized and potentially disruptive technology scanner that could greatly ease both the cost and burden of a field-forward instrument purpose-built for TBI imaging. This Halbach imager contrasts markedly with the electromagnetic LFI in that it has a highly inhomogeneous magnetic field, but we use this inhomogeneity to our advantage.

to our advantage as an encoding field to acquire head images without the use of an additional gradient set.

Halbach array (permanent magnet) LFI

This test bed scanner is based around a lightweight array of permanent magnets in a so-called Halbach configuration. This magnet is ideal for portable MRI in that it creates a relatively uniform field transverse to the head without the use of a cryostat or power supplies. This Halbach array scanner is a highly specialized scanner and a potentially disruptive technology that could greatly ease both the cost and burden of a field-forward instrument purpose-built for TBI imaging. This Halbach imager contrasts markedly with the electromagnetic LFI in that it has a highly inhomogeneous magnetic field, but we use this inhomogeneity to our advantage and use it to acquire head images without the use of an additional gradient set.

A truly portable MR system has the potential to quickly detect brain injury at the site of injury. For example hemorrhage detection is critical for both stroke patients and traumatic brain injury victims. In stroke, rapid distinction between a hemorrhagic and non-hemorrhagic event could allow administration of a clot-busting drug such as tPA (tissue plasminogen activator) in an ambulance prior to transportation to the hospital, perhaps advancing this time-sensitive treatment

by up to an hour. Subdural hemorrhage (or hematoma) is a form of traumatic brain injury, in which blood gathers between the dura and arachnoid mater (in meningeal layer) and is likely to be visualized on course resolution (e.g. 5 mm) T1 images.

In Y1 we designed and built the very portable 45 kg Halbach array magnet for portable MRI, and mapped the magnetic field and drift using NMR measurements at 3.3 MHz. In Y2 we focused on the hardware and encoding techniques needed to turn this magnet into an imager. In Y3, we solved some critical challenges including the ability to acquire 2D multi-channel images. Research in 2014 (Y4) saw substantial progress toward the acquisition of true 3D datasets in the Halbach magnet portable imaging prototype [1]. For the first time, three key ingredients – “built-in” 2D encoding using a rotating B_0 encoding field, phase encoding with a linear phase RF transmit coil, and broadband RF pulses – were brought together to enable three-axis encoding in an inhomogeneous B_0 field with no gradient coils.

Halbach array LFI: extension to 3D encoding

Previously in 2013, we achieved 2D axial-plane imaging without gradient coils by using a rotating, 45 kg, 77 mT inhomogeneous Halbach cylinder based magnet. The built-in field variation of the permanent magnet array was used as a rotating spatial encoding magnetic field (rSEM). As the magnet rotates around the sample, generalized projections onto the non-linear SEM are acquired as a spin echo train. Images (Figure 1) are reconstructed from the projection data by applying an iterative solver to the full encoding matrix calculated using the signal equation [1].

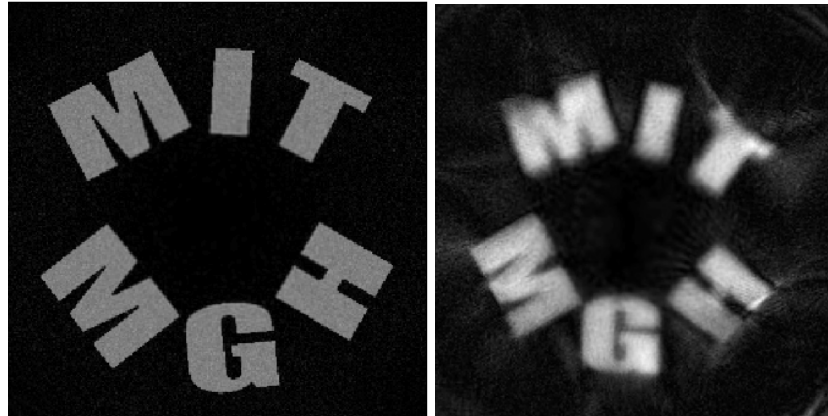


Figure 1: Ground truth phantom with text (left) contained in a 1.5cm thick cylinder slab. 2D imaging based on Halbach rSEM data is shown at right. Parallel receive coils are used to disambiguate the non-bijective mapping of the nonlinear encoding field.

TRASE encoding

To enable imaging in the 3rd direction (along the axis of the cylindrical magnet, see Figure 2), we use the Transmit Array Spatial Encoding (TRASE) method [2], [3]. TRASE is a B_1^+ encoding method that requires 2 different switchable B_1^+ phase gradients (often equal and opposite) along the encoding direction. The 1D TRASE sequence (Figure 3) is a modified RARE spin-echo train in which the slope of the B_1^- phase gradient switches for consecutive refocusing pulses (indicated by the + or -). The two phase gradients correspond to two k -space origins ($-k_1$ and k_1), and the previous k -space point is flipped across the k -space origin of the refocusing pulse to traverse k -space. With each successive pulse in the echo train, the object is modulated by additional Δk_1 until sufficient spatial encoding is achieved.

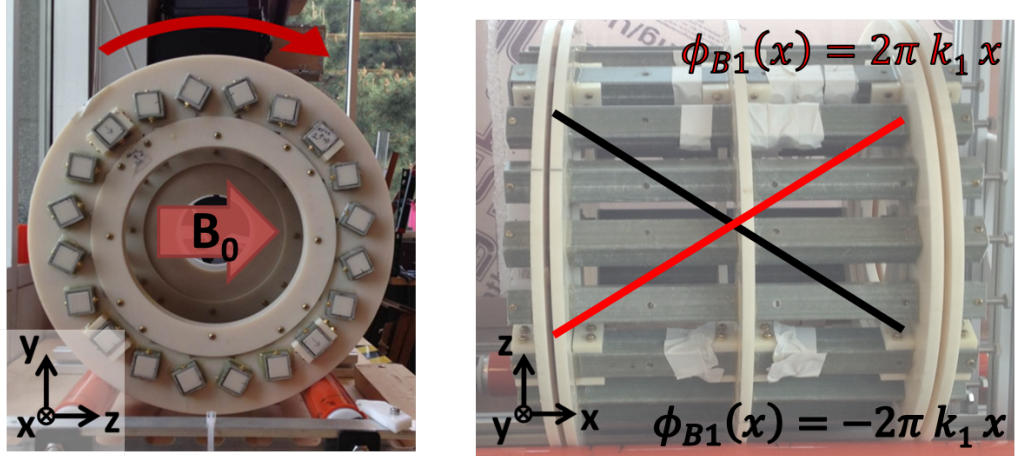


Figure 2: (a.) Y-Z encoding is performed with the rotating SEM method. (b.) TRASE is implemented in the X direction using a switchable linear B_1^+ phase along X.

Coil hardware

A TRASE array was designed that consists of two nested cylindrical coils (Figure 4). Coil 1 is a short 4-turn birdcage coil (12 rungs, 18cm diam., 22cm length) [4] that produces a B_1^+ field in \mathbf{Y} with a cosine shape along \mathbf{X} , $B_{1y}^+(x) = |B_{1xy}^+| \cos(2\pi k_1 x)$. Coil 2 is a 10 turn Maxwell coil (22cm diam., 18cm length) that produces a B_1^+ field in \mathbf{X} with a sine shape along \mathbf{X} , $B_{1x}^+(x) = \pm |B_{1xy}^+| \sin(2\pi k_1 x)$.

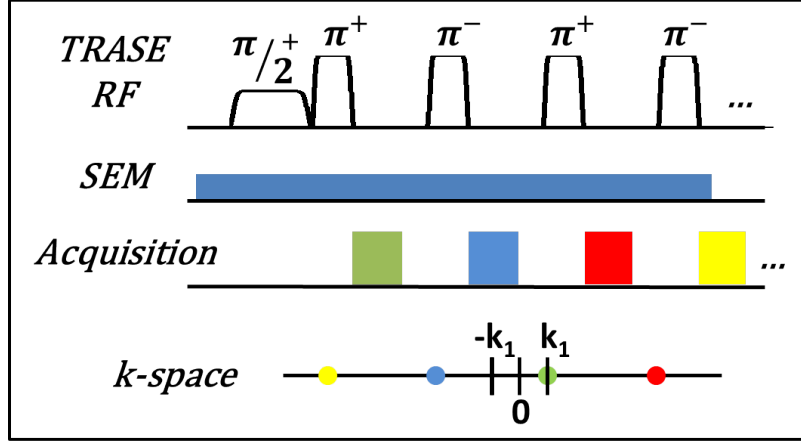


Figure 3: The TRASE sequence is repeated for every magnet rotation of the imaging sequence. The +/- indicates the sign of the TRASE phase slope.

The coils are tuned to the Larmor frequency (3.29 MHz) and decoupled with a transformer (-20 dB isolation). Figure 4b shows the relative magnitude of B_{1x} and B_{1y} from the 2 coils measured with a pick-up loop. When the two coils are driven with equal $|B_{1xy}^+|$ magnitude and spatial frequency, k_1 , they produce the desired B_1^+ field variation along X, $B_1^+(x) = |B_{1xy}^+|e^{+i2\pi k_1 x}$ (uniform magnitude and linear phase). A switchable 180° phase shifter is added in the Maxwell coil RF path, which applies a sign change to every other refocusing pulse. The pulses with the phase shift thus have a negative phase gradient; $B_1(x)^+ = |B_{1xy}^+|e^{-i2\pi k_1 x}$.

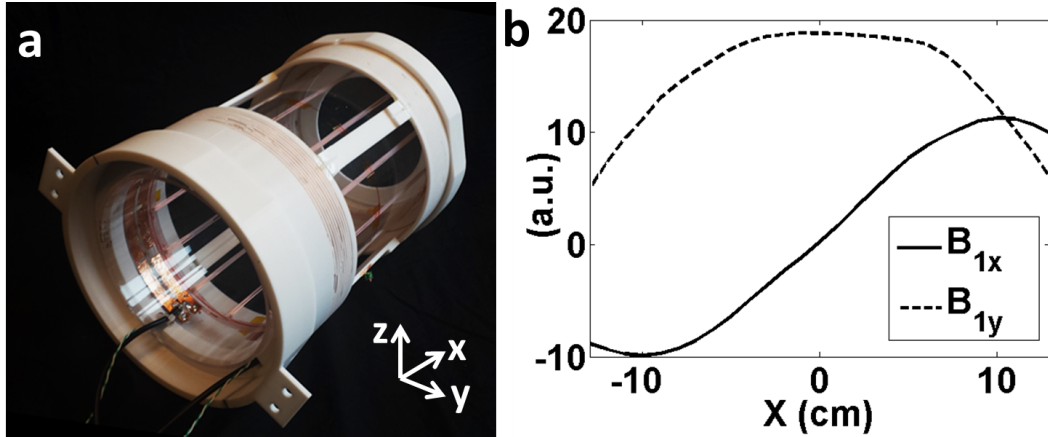


Figure 4: The TRASE array is a nested birdcage and Maxwell coil. b: The measured magnitude from B_{1x} of the Maxwell coil and B_{1y} of the birdcage coil is plotted

Acquisition

The 2D rSEM method and TRASE are performed simultaneously for 3D imaging. The TRASE array must rotate with the magnet because the Y direction changes as the magnet rotates. For every magnet rotation, the projection onto the SEM is acquired as a TRASE-modulated 16-echo

spin-echo train (each echo: readout = 196 pt, BW = 40 KHz, echo spacing = 9.7 ms). Data is acquired at 180 rotations of the magnet spaced 1° apart. Frequency-swept WURST pulses are used to achieve the same flip angle across the inhomogeneous field (BW = 25 KHz, [pw90, pw180] = [6,3] ms) [5]. The birdcage coil of the TRASE array is used as the receiver coil.

Correction of quadratic phase from frequency-swept pulses

It is difficult to perform TRASE encoding using short, rectangular “hard” pulses in the presence of the Halbach inhomogeneous ΔB_0 SEM due to practical limitations on the available RF power, and thus the minimum achievable refocusing pulse duration. The TRASE point spread function degrades rapidly for refocusing pulse angles outside the range 150-195° due to the accumulation of flip angle and phase errors along the echo train [6]. For the hard pulses used in early published TRASE images [2] the refocusing angle falls below 150° when $\Delta B_0 > 40\%$ of the pulse Rabi frequency.

To overcome this limitation, we perform TRASE in the presence of strong off-resonance using WURST-40 pulses [7] with phase cycling [5] for accurate spin excitation and refocusing across also isochromats. Pulses with a linear frequency sweep impart a quadratic phase across the spin bandwidth, but if the pulse sweep rate satisfies the condition $R_{exc} = \frac{1}{2} R_{ref}$ and the ΔB_0 SEM is constant over time, then the refocusing pulse removes the phase applied by the excitation pulse and all isochromats refocus the echo time [8]. Further readouts in the echo train alternate between echoes and “spectral” echoes [5] that resemble the frequency distribution of spins in the ΔB_0 SEM. This additional RF phase modulation must be removed to make the spectral echoes compatible with TRASE.

The spectral echo signal can be modeled as a convolution of the conventional spin echo signal with a chirp function, $\exp(i2\pi\beta t^2)$, where β depends on the sweep rate. Deconvolution is performed by either (a.) convolving the spectral echo with a scaled, conjugated version of the chirp function, or equivalently (b.) in the Fourier transform domain by dividing the FFT of the echo (1D projection) by the FFT of the chirp function [9]. Since the FFT’ed chirp kernel is a pure phase term, method (b.) requires simply taking the difference between the phase of the first and second projections from the echo train (Figure 5). This phase difference is used to correct all subsequent spectral echoes.

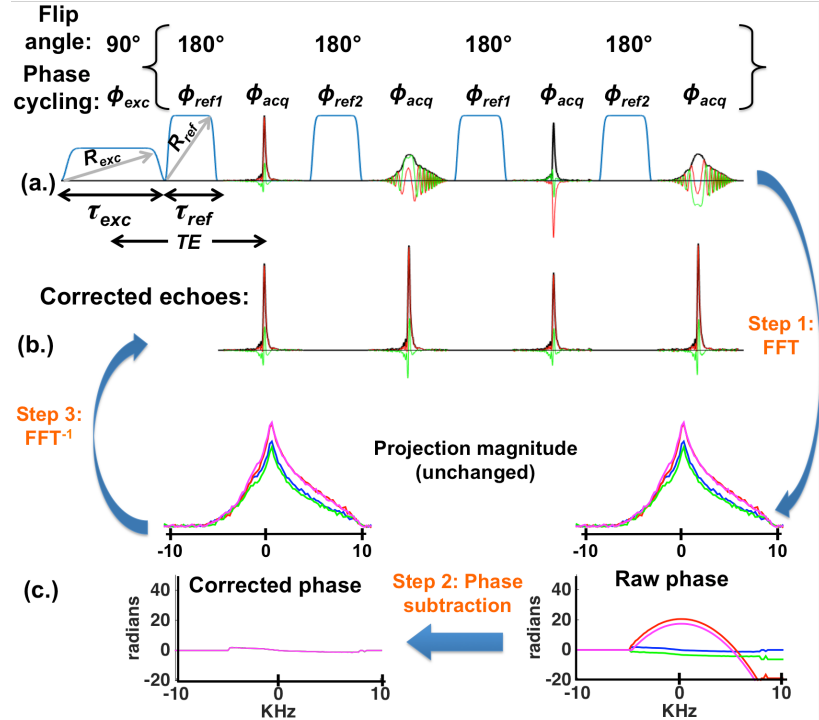


Figure 5: WURST pulse sequence diagram with four echoes acquired on a water bottle phantom. The bracketed block is repeated as needed. Conventional echoes alternate with “spectral” echoes modulated by the quadratic phase of the frequency swept RF pulses. This effect is compensated by the removal of the quadratic phase from the projections corresponding to each spectral echo. After phase correction, the echo real and imaginary parts overlay for all echoes in the train. Phase cycling scheme is as follows: $\phi_{exc} = [90, 270, 180, 0]^\circ$, $\phi_{ref1} = [0, 0, 90, 90]^\circ$, $\phi_{ref2} = [90, 90, 0, 0]^\circ$, $\phi_{acq} = [0, 180, 90, 270]^\circ$. The 3rd and 4th echoes in the block are multiplied by π to compensate for phase cycling.

To validate the phase correction method, a 1D multi-tube phantom is placed in the Halbach ΔB_0 SEM and a train of echoes is acquired using TRASE. WURST-40 excitation and refocusing pulse durations are $[\tau_{exc}, \tau_{ref}] = [6, 3]$ ms and sweep rates are $[R_{exc}, R_{ref}] = [4.15, 8.3]$ MHz/s over a 25 KHz bandwidth.

Fourier domain phase subtraction faithfully restores spectral echoes so that their real and imaginary components align closely with those of conventional echoes (Figure 6). The TRASE acquisition successfully generates projections of the phantom even though its bandwidth exceeds 10 KHz in the ΔB_0 SEM. By contrast, recognizable projections could not be obtained using hard pulses since available RF power constrained the minimum pulse duration to [75,150] μ s for [90°,180°] pulses, providing inadequate bandwidth.

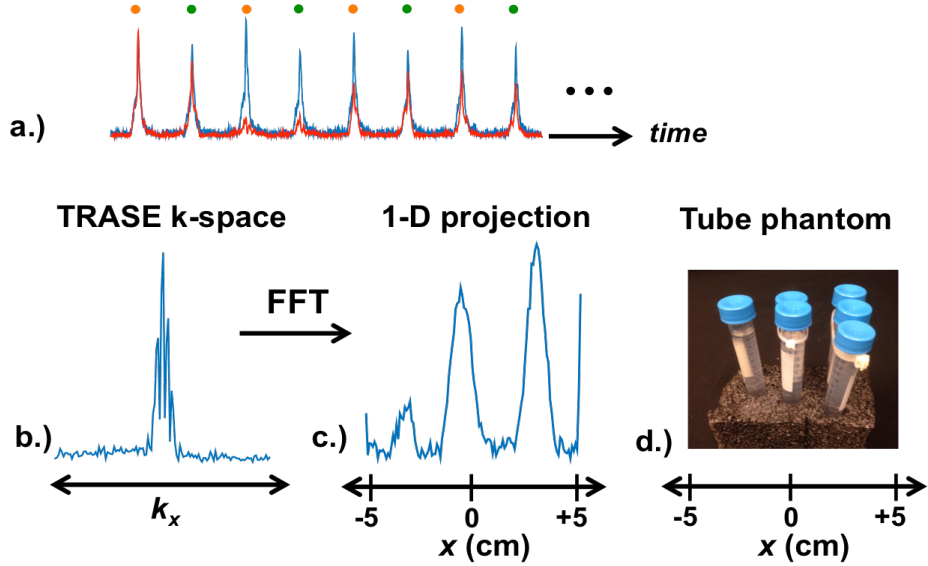


Figure 6: The first 8 corrected echoes (a.) from an echo train shown with (red) and without TRASE phase modulation. Orange and green dots at each echo time denote positive and negative k-space points, respectively, which are reordered into 1D k-space (b.) The Fourier transform yields a 1D projection (c.) of the water-filled tube phantom (d.).

3D Reconstruction

Once the raw data are phase corrected as described above, image reconstruction proceeds. **Step one** separates the echo train data along **X** to obtain 16 different **YZ**-datasets corresponding to each slice. For each point in the readout window, the set of 16 points along the echo train populates a k-space vector (Figure 3). The points are rearranged and FFT’ed to generate a 1D projection along **X** (Figure 6 and Figure 7). Only the k-space lines formed from the center points of the echoes result in 1D projections that are not modulated by the B_0 SEM. This is repeated for the echo trains from each of the magnet rotations. **Step two** reconstructs each set of echoes (**YZ**-data) into a 2D image of the corresponding slice. The encoding matrix for each slice is calculated using 2D B_0 field maps and then iterative matrix inversion is performed to separately obtain each 2D image.

Results:

Figure 7 shows experimental 3D imaging results using a 7.5 cm thick phantom with 1.5 cm water-filled compartments spaced 3cm apart in **X**. A 1D projection along **X** shows the water-filled compartments. Three slices are reconstructed from data at $\mathbf{X} = [-3\text{cm}, 0\text{cm}, 3\text{cm}]$ using the corresponding 2D ΔB_0 field maps.

Discussion

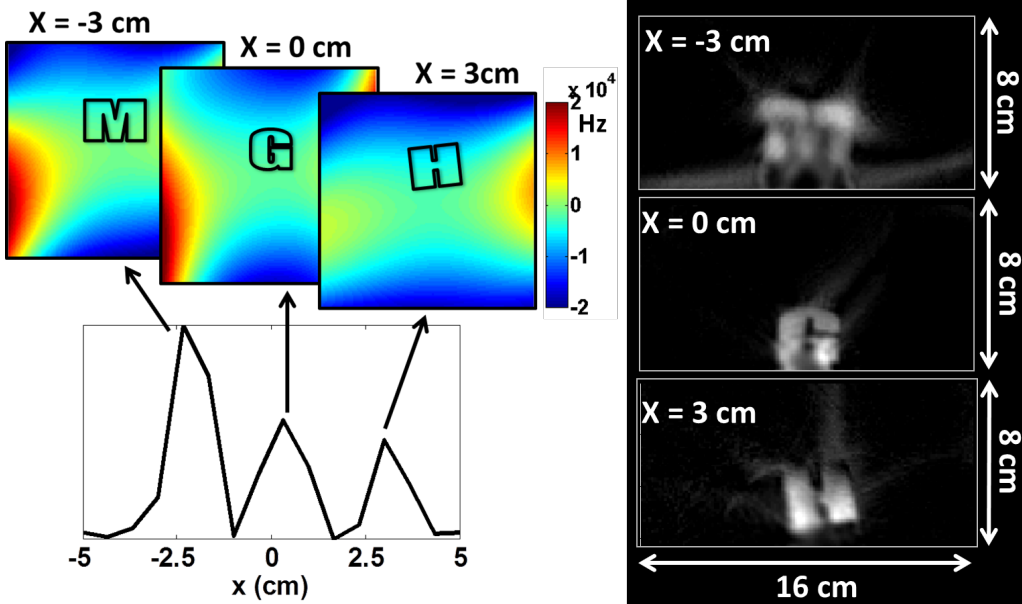


Figure 7: Image of a 3D phantom consisting of three water-filled compartments spaced 3 cm apart in X. A 1D projection along X for one rotation angle is shown. Three image slices were reconstructed using the appropriate 2D field maps.

The non-bijectivity of the SEMs results in image aliasing across the center. This is usually resolved using a surface coil array [10], but as a first step, the birdcage coil of the array is used for a receiver coil and only the reduced FOV image is shown. The blurring in the image slice is due to a combination of the spatially varying resolution of the SEMs and systematic calibration errors in our model-based reconstruction.

We have demonstrated proof-of-concept 3D images in the inhomogeneous 45 kg Halbach magnet without the use of gradient coils. TRASE encoding along X is ideal because like our 2D method it uses spin echo trains, and it avoids the need for a B_0 gradient coil and gradient power amplifier, which would add weight, cost, and power requirements to the portable, low-cost system.

We have further shown that robust TRASE spatial encoding in an inhomogeneous B_0 field can be achieved using frequency-swept WURST pulse echo trains when a simple correction method is used to remove the unwanted quadratic phase from alternate echoes.

High-efficiency helmet detectors for the electromagnet LFI

MRI at low magnetic field (<10 mT) without cryogenic or hyperpolarization techniques presents unique engineering challenges. Imaging coils must maximize coverage over the volume of interest while minimizing losses in a regime unusual in contemporary MRI—where Johnson noise dominates the noise floor. Our previous work validated our scanner hardware and pulse sequences MRI at 6.5 mT. The purpose of the present work is to construct a high-performance coil for low-field imaging of the human brain *in vivo*.

Spiral volume helmet detectors: receive coil development

Our previous coils focused on implementing array coil technology common at clinical field strengths, and we constructed an 8 channel receive-only coil for our 6.5 mT low-field imager at 276 kHz. While our results were promising [11], [12], a lack of low noise high-impedance pre-amplifiers at our frequency regime prevented us from achieving sufficient coil decoupling, resulting in images with poor SNR. We present here a single channel coil with greatly improved SNR for these applications.

We designed a spiral volume coil design for combined Tx and Rx and optimized for human head imaging in the transverse B₀ field of our low field scanner. This places the receive element close to the head while still covering the entire volume uniformly. Additionally, the symmetry of a spherical spiral results in a homogeneous magnetic field over its volume, minimizing B₁ inhomogeneity [13], [14]. Losses in low field imaging are mainly due to resistive losses in the coil (the so-called Johnson noise regime). Rather than lower this resistance by cooling, we instead use of multistranded Litz wire. When compared to a solid copper wire of the same gauge, a loop made of Litz wire will have the same inductance but a fraction of the AC resistance, resulting in a lower noise floor and higher image SNR.



Figure 8: Form fitting helmet with 30-turn spiral design.

The optimal number of turns and appropriate wire gauge were determined through simulation. The helmet shape was designed to fit closely to an anatomically accurate human head model.

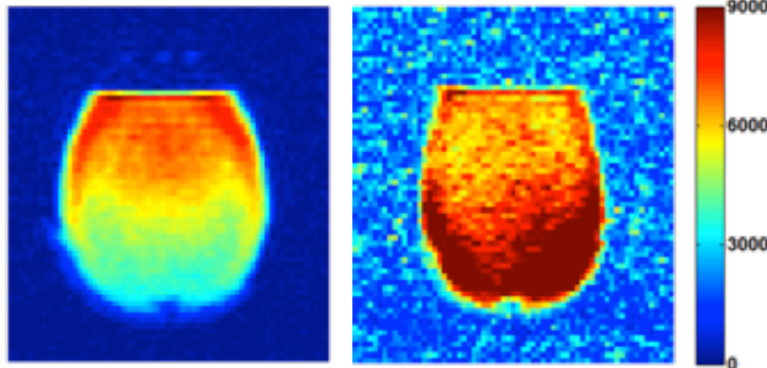


Figure 9: Equivalent slices in a head phantom acquired using the single channel spiral coil (A) and the 8-channel array (B) at 6.5 mT. Images are scaled by their maximum intensity.

BW=6 kHz.

From simulations, we built a 30-turn spiral wound with Type 1 40/38 Litz wire. Our aligned turn-to-turn spacing was 5.6 mm. The final design was 3D printed using fused deposition modeling technology with polycarbonate in a Fortus 360 mc printer (Stratasys, Eden Prairie, MN, USA), (Figure 8).

Images were acquired at 6.5 mT in a head shaped phantom using 3D b-SSFP with 50% undersampling. Resulting voxel size was $3.9 \times 3.5 \times 16.7$ mm 3 (NA=110) (Figure 9a). A maximum in-plane SNR of 130 was calculated. An image of a similar slice obtained with the 8-channel array coil is shown for comparison (Figure 9b, combined image using RSS, voxel size = $4.4 \times 4.2 \times 22$ mm 3 , NA = 80, max SNR = 16.5).

18 slices of a head-shaped structured resolution phantom imaged with optimized spiral volume coil are shown in Figure 10. This four-quadrant phantom is filled will liquid-filled spheres of various diameters. Voxel size in this scan is $3.5 \times 2.5 \times 5$ mm 3 with NA=40 and maximum SNR of 24.8. Total acquisition time is 10 minutes.

The spiral path was generated in a custom MATLAB (Mathworks Inc.) script and imported into BiotSavart (Ripplon Software Inc.) for an estimate of inductance. Resistance was computed from the estimated wire length and the characteristic impedance per length of wire for that gauge. Coil Q was estimated as wL/R . Bandwidth was estimated from the Q value. We iterated through several designs until we achieved our target Q~40 and

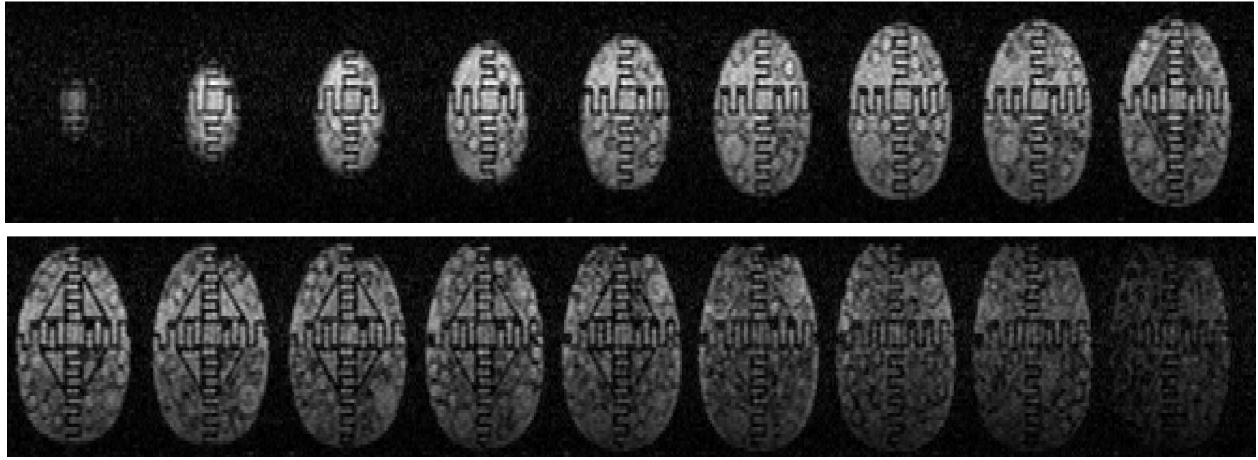


Figure 10: Axial view of a multi-compartment head-shaped phantom acquired with the Litz spiral volume coil at 6.5 mT in 10 minutes.

This 30-turn single channel volume spiral coil designed for low field imaging significantly outperformed our 8-channel array coil. By minimizing losses in the coil, maximizing filling factor and eliminating coupling issues, we were able to obtain significantly higher SNR. We have successfully designed and constructed a high filling factor human-head Tx/Rx spiral volume imaging coil for 6.5 mT (276 kHz).

OMRI Injury Imaging

TASK 2A: OMRI Hardware Development

Overhauser-enhanced MRI (OMRI) is an electron-proton double resonance imaging technique of much interest due to its ability to detect the concentration and distribution of free radicals. Tracking of exogenous free radicals with OMRI *in vivo* has enabled the development of oxymetry probes [15] and the imaging of redox reactions [16]. The large gyromagnetic ratio of electrons (28 GHz/T) demands that *in vivo* OMRI is performed at very low magnetic fields (\sim 10 mT) in order to minimize RF heating and penetration depth issues. Operation at low magnetic field causes a drastic reduction in NMR sensitivity despite the signal enhancement that comes from the Overhauser effect, and emphasizes the need for high S/N probes. OMRI probe design is still relatively unexplored, despite its importance, and presents challenges unique to the frequencies of operation ($f_H = 276$ kHz and $f_e = 140.8$ MHz in our experiments at 6.5 mT).

A key challenge in implementing OMRI for TBI will be detecting the small concentrations of radical present *in vivo*. We have previously shown that 10 μ M nitroxide radical in water and 50 μ M nitroxide radical in water can be detected with Overhauser spectroscopy (Figure 11) and OMRI (Figure 12), respectively. The concentration of free radical at the location of injury re-

mains *unknown*, but estimates range from 50 nM to 50 μM [17]-[24]. Additionally, detecting free radicals *in vivo* will be more difficult than in phantoms due to extra relaxation pathways reducing the efficiency of DNP. Therefore we would like to try and improve our detection efficiency even further.

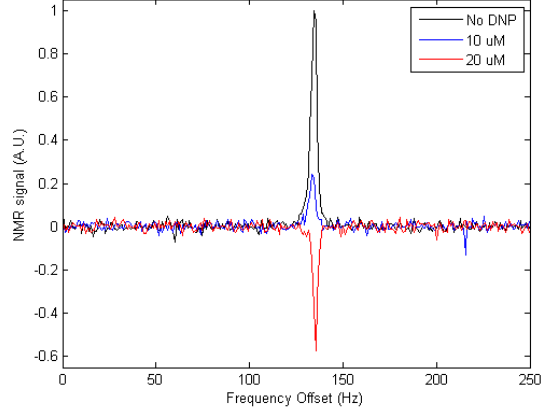


Figure 11: Measurement of the sensitivity threshold to small concentrations of nitroxide radical via Overhauser enhanced NMR spectroscopy. These spectra were acquired in the electromagnet LFI at 6.5 mT (276 kHz). The ESR frequency was 140 MHz.

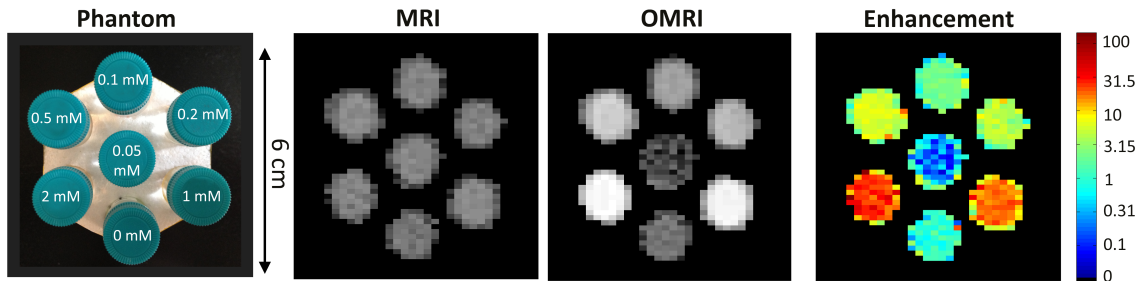


Figure 12: Photograph of phantom used to demonstrate the sensitivity of OMRI to nitroxide radical concentration. All seven vials have very similar image magnitudes in the conventional MRI image. The OMRI scan demonstrates marked image-based free radical sensitivity. The signal magnitude from the control vial remains unchanged in OMRI scan. **OMRI enhancement** image is computed from the ratio of OMRI to MRI magnitude. MRI and OMRI were both obtained at 6.5 mT. The NMR frequency is 276 kHz and the ESR frequency is 140 MHz.

Improving radical detection sensitivity through double resonator design

We report here the development of a high performance OMRI probe with broad tunability, capable of imaging enhancement over a wide range of free radical electron g -factors. This OMRI

probe was developed because it was determined that significant improvement in our OMRI hardware were needed before we could attain sensitivity to superoxide. We have developed an OMRI probe consisting of an NMR solenoid inside a modified Alderman-Grant Resonator (Figure 13), to interfaces with the 6.5 mT electromagnet LFI ($f_H = 276$ kHz). Images were acquired using our recently developed, fast, high-resolution b-SSFP based OMRI methodology [25]. NMR probe design in the low-field regime is fundamentally different to that at conventional MRI fields as thermal noise due to the intrinsic resistance of the pickup coil dominates over sample noise. This leads to a compromise where S/N improvements come at the expense of imaging bandwidth $S/N \sim \sqrt{Q} \sim 1/\sqrt{BW}$. An 85 turn solenoid was wound, using low AC resistance 5/39/42 litz wire, on a 3D printed polycarbonate former. This high filling factor coil has a bandwidth of 3 kHz.

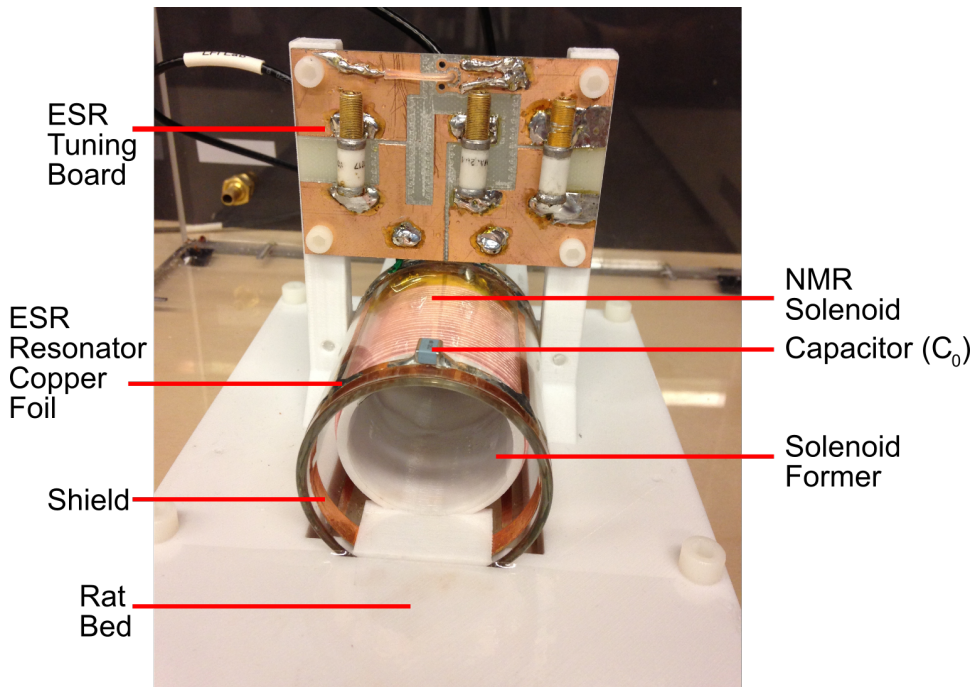


Figure 13: NMR/ESR rat head probe for operation at 6.5 mT. The ESR resonator is tuned to 140.8 MHz. The litz wire NMR solenoid coil (276 kHz) resonator board is not shown.

A modified Alderman-Grant ESR resonator was built using copper foil on Pyrex tubing. All metal placed in close proximity to the NMR solenoid strongly couples, reducing the NMR sensitivity. We therefore minimized amount of copper in the ESR resonator. Windows were removed from the panels on the sides of an Alderman-Grant resonator, a region of low current flow [26], in an attempt to reduce coupling whilst maintaining B_1 homogeneity. Shielding at the ends of the resonator prevents high electric fields at the capacitors penetrating the imaging volume, important because $P_{RF\text{-absorbed}} \sim E^2$. Slits in the shielding prevent the formation of closed loops that couple to

the solenoid. Figure 14 demonstrates the high B_1 homogeneity and strong E suppression in our ESR resonator.

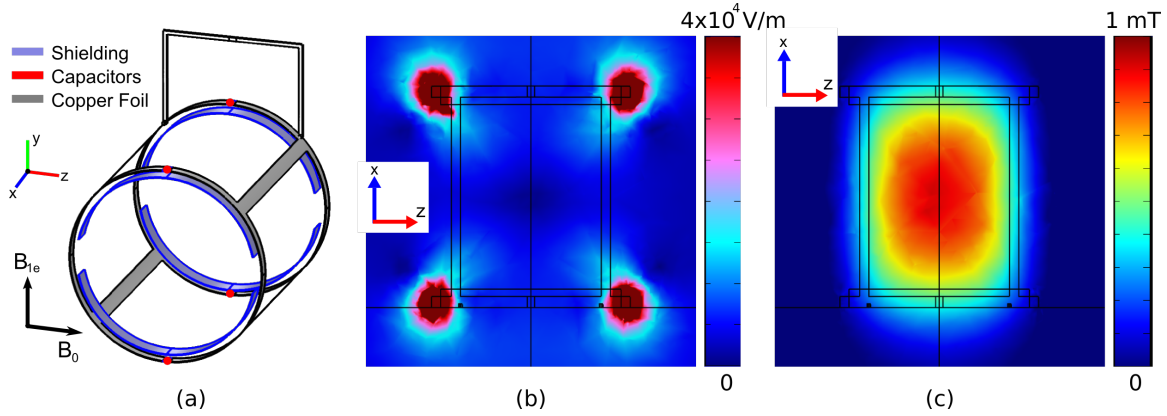


Figure 14: COMSOL Multiphysics simulations (a) Our modified Alderman-Grant Resonator. (b) Plot of $|E|$ showing that the electric field is strongly suppressed inside the resonator. (c) B_{1e} shows high homogeneity in the imaging volume – less than 10% variation across the imaging region.

TEMPO (4-hydroxy-TEMPO) a stable radical, is detected by OMRI with high sensitivity, and because of its small size may facilitate imaging blood brain barrier leakage in cases of oxidative stress [27]. Simulations were validated in 2 mM TEMPO solutions using simple spectroscopic measurements as well as fast imaging strategies [25]. The ESR resonator was tuned to 141 MHz, the lowest frequency of the TEMPO triplet state at 6.5 mT, to minimize RF heating during ESR irradiation.

In vivo performance

Previously we described the development of an OMRI probe for a rat head model utilizing an NMR solenoid and ESR surface coil. Testing of this new OMRI probe indicates that it has $3\times$ the S/N of the probe reported [27], and rectifies problems with B_{1e} homogeneity, yielding homogeneous enhancement of -6.7 in 2 mM TEMPO when 10 W of RF power is applied. *In vivo* OMRI signal enhancement is clearly visible in the rat brain after TEMPO injection, as shown in Figure 15. As the Overhauser-enhanced signal has a phase opposite to that of the thermal signal, the phase image in Figure 15 provides sensitive contrast in regions of low TEMPO concentration.

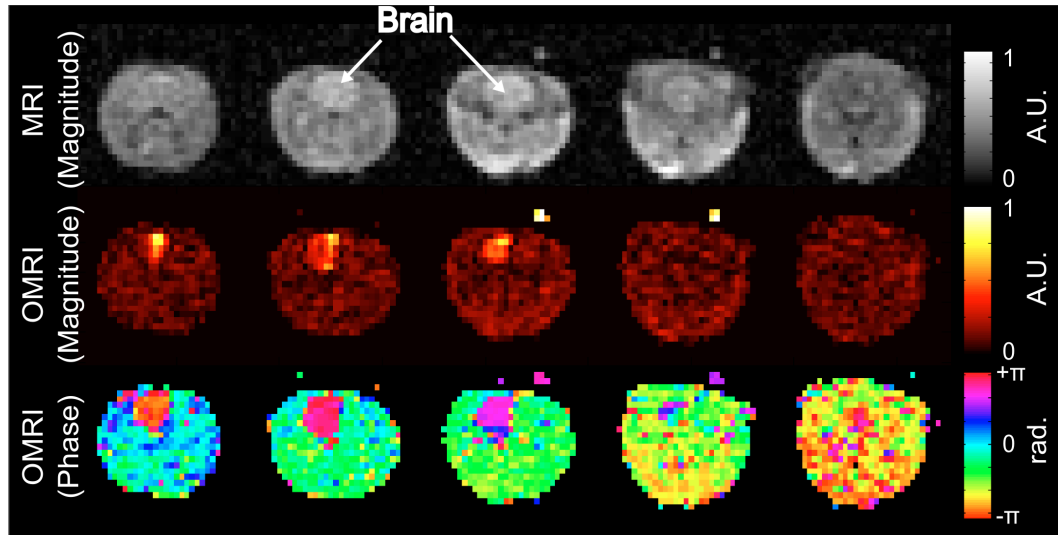


Figure 15: OMRI images acquired from a rat at 6.5 mT following injection of 1 mL of 150 mM TEMPOL. Five slices from an 11 slice data set shown. OMRI (NA=1) imaging time was **9 seconds**. Anatomical MRI (NA=30) was acquired in the OMRI scanner with ESR power disabled. All images, voxel size: $1.1 \times 1.6 \times 8 \text{ mm}^3$, Matrix: $128 \times 35 \times 11$. A fiducial containing 2 mM of TEMPOL was placed outside the animal and is seen in both MRI and OMRI images.

In summary, we have implemented a high performance probe for high temporal and spatial resolution OMRI and demonstrated it *in vivo* in the brain of living rats. The S/N of this probe may be further improved, whilst maintaining imaging bandwidth, by using an active feedback circuit [28]. Higher S/N could also be realized through supercooling of the NMR solenoid or by using a free radical with a longer T_{1e} such as triphenylmethyl [15]. This probe may allow the *in vivo* detection of rapid redox changes in pathologic tissues, specifically in the context of brain trauma or stroke.

KEY RESEARCH ACCOMPLISHMENTS:

Electromagnet 6.5 mT LFI:

- Designed, constructed, and characterized optimized high-efficiency single channel spiral “helmet” for human head imaging at 6.5 mT
- Designed and built new multi-compartment head-shaped imaging phantom
- Acquired high-quality images from multi-compartment phantom using human head coil $2.5 \times 3.5 \times 5 \text{ mm}$ resolution (18 slices) in 10 minutes

Permanent magnet Halbach LFI:

- Simulated TRASE array to enable 3D encoding

- Designed and built TRASE array coils with switchable 180° phase shifter
- Implemented 3D encoding using simultaneous 2D rSEM and TRASE
- Implemented WURST-40 acquisition to mitigate quadratic phase from frequency-swept pulses
- Demonstrated proof-of-concept 3D imaging in the inhomogenous 45 kilogram Halbach magnet without the use of gradient coils.

Overhauser MRI in electromagnet LFI:

- Established collaboration with D. Whitney King (Colby College) to provide superoxide generator for OMRI sensitivity calibration
- Developed and built high performance OMRI/MRI probe with wide-range OMRI tuning and low SAR, and 3-fold improved MRI SNR.
- Acquired 11 slice, $1.1 \times 1.6 \times 8$ mm in-plane resolution MRI (4.5 minutes) and OMRI (9 seconds) in rats
- Developed methodology to measure dynamic time resolved OMRI *in vivo*

REPORTABLE OUTCOMES:

1. C LaPierre, M Sarracanie, B D Armstrong, J Polimeni, and M S Rosen, Overhauser-enhanced MRI with SENSE Acceleration in the Johnson Noise Dominated Regime, presented at the 55th Meeting of the Experimental NMR Conference, Boston, MA, March 23-28 2014.
2. M Sarracanie, B D Armstrong, and M S Rosen, High Speed MR Fingerprinting at 6.5 mT, presented at the 55th Meeting of the Experimental NMR Conference, Boston, MA, March 23-28 2014.
3. M Sarracanie, P Stanwix, and M S Rosen, A Single Channel Variable Density Spiral Coil for High Sensitivity MRI at 6.5 mT, presented at the 55th Meeting of the Experimental NMR Conference, Boston, MA, March 23-28 2014.
4. C Z Cooley, J P Stockmann, M Sarracanie, B D Armstrong, M S Rosen, and L L Wald, 2D Imaging in a Portable MRI Scanner without Gradient Coils, presented at the 55th Meeting of the Experimental NMR Conference, Boston, MA, March 23-28 2014.
5. C LaPierre, M Sarracanie, L L Wald, and M S Rosen, An Optimized 8-Channel Helmet Array for Head Imaging at 6.5 mT, presented at the 55th Meeting of the Experimental NMR Conference, Boston, MA, March 23-28 2014.

6. C Z Cooley, J P Stockmann, B D. Armstrong, M Sarracanie, M S. Rosen, and L L. Wald, Spatial resolution in rotating Spatial Encoding Magnetic field MRI (rSEM-MRI), presented at the 22nd Meeting of the International Society of Magnetic Resonance in Medicine, Milan, Italy May 10-16 2014.
7. C LaPierre, M Sarracanie, B D. Armstrong, J R Polimeni, and M S. Rosen, Overhauser-enhanced MRI with SENSE Acceleration in the Johnson Noise Dominated Regime, presented at the 22nd Meeting of the International Society of Magnetic Resonance in Medicine, Milan, Italy May 10-16 2014.
8. C LaPierre, L L Wald, and M S. Rosen, An Optimized 8-Channel Helmet Array for Head Imaging at 6.5 mT, presented at the 22nd Meeting of the International Society of Magnetic Resonance in Medicine, Milan, Italy May 10-16 2014.
9. M Sarracanie, B D. Armstrong, and M S. Rosen, High Speed MR Fingerprinting at 6.5 mT, presented at the 22nd Meeting of the International Society of Magnetic Resonance in Medicine, Milan, Italy May 10-16 2014.
10. M S Rosen, invited talk, “New methods of low-field MRI for application to TBI”, Invited talk, TBI Neuroimaging Meeting, US Army Medical Research and Materiel Command and Defense Centers of Excellence for Psychological Health and Traumatic Brain Injury, Fort Detrick, 30 Jan 2014.
11. M S Rosen, invited talk, “Overhauser-enhanced MRI as a Non-invasive Probe of BBB Breakdown and Redox State in Stroke”, 55th meeting of the Experimental NMR Conference, Boston, MA, 27 Mar 2014.
12. M S Rosen, invited talk, “Overhauser-enhanced MRI as a Non-invasive Probe of BBB Breakdown and Redox State in Stroke”, 22nd Meeting of the International Society of Magnetic Resonance in Medicine, Milan, Italy, May 10-16 2014.
13. M S Rosen, invited seminar, “High-performance Low-field MRI: Brain Imaging & Free Radicals”, Psychiatry Neuroimaging Laboratory seminar, Brigham and Women’s Hospital, Boston MA, 22 June 2014
14. M S Rosen, invited talk, “Low-field MRI for Non-invasive imaging of brain function”, NSF Workshop on Noninvasive Imaging of Brain Function, Arlington, VA, 23 July 2014.
15. **Seven abstracts accepted for presentation in 2015** that result from research presently funded in the Rosen lab by DoD/DMRDP are attached below as **Appendices 2–8**.

16. CZ Cooley, JP Stockman, BD Armstrong, M Sarracanie, MH Lev, MS Rosen, and LL Wald, "2D Imaging in a Lightweight Portable MRI Scanner without Gradient Coils", published in *Magnetic Resonance in Medicine*, 2014, attached as **Appendix 9**.
17. MGH/Partners provisional patent MGH-22726, (Mar 14, 2014). This patent describes optimized receive arrays for parallel imaging in the Johnson noise dominated regime. **LICENSED**
18. MGH/Partners provisional patent MGH-22727, (Mar 14, 2014). This patent describes Overhauser-enhanced MRI (OMRI) is used in combination with an exogenously administered free radical probe to (for example) tomographically probe blood brain barrier breakdown and tissue oxidative stress status *in vivo*.
19. MGH/Partners provisional patent MGH-22728, (Mar 14, 2014). This patent describes a new efficient method for high-speed Overhauser MRI (OMRI) where ESR irradiation is applied within the TR of a conventional MRI pulse sequence, typically during the phase-encode part of the sequence. **LICENSED**.
20. MGH/Partners provisional patent MGH-22729, (Mar 14, 2014). This patent describes the use of a variable density spiral design to provide homogeneous magnetic field and high sensitivity over broad regions of interest when used for either transmit, receive, or both.
21. MGH/Partners provisional patent MGH-22730, (Mar 14, 2014). This patent describes a new form fitting spiral coil design to provide homogeneous magnetic field and high sensitivity over three-dimensional volumes. **LICENSED**.
22. MGH/Partners provisional patent MGH-22731, (Mar 14, 2014). This patent describes a new approach to Magnetic Resonance Fingerprinting (MRF) whereby a user defined fraction (including the whole) of k -space is acquired in a sequential fashion, in two or three dimensions.
23. Funding obtained (2014): NIH R21 NS087344-01 (PI Rosen), "Non-invasive Free Radical MRI in Stroke".
24. Funding obtained (2014): NIH R01 EB018976-01 (PI Wald), "Technology for Portable MRI".
25. Funding applied for: DARPA Seedling (PI Rosen), 2014.
26. Funding applied for: Joint Warfighter Medical Research Program (PI Rosen), 2014.
27. Funding applied for: DOD BAA (PI Rosen), 2014.

CONCLUSION:

The reason MRI is not widely deployable is that high-strength magnetic fields (of order 1 T) are necessary with conventional MRI to obtain useful brain images. Such high field scanners involve large, heavy, fragile, expensive equipment (such as superconducting magnets) that are difficult to site in field hospitals. We contend that low-magnetic-field implementations of MRI can be developed to allow robust, transportable imaging modalities well suited to diagnose the types of battlefield injuries prevalent in TBI and practical for operation in field hospitals. Application of the suite of techniques and technologies from our work could advise future development of a deployable device with a high diagnostic impact and could be transformative, enabling improved diagnosis and monitoring of battlefield injuries prevalent in TBI.

The electromagnet LFI provides an ideal state-of-the art test bed for all of the novel acquisition, detection methodologies, and reconstruction algorithms including navigators and sparse sampling, and additionally will provide necessary experience and data to advise optimal construction and magnetic field for any future electromagnet-based deployable systems. In its current configuration, this state-of-the-art scanner enables high-performance spectroscopy and 8-channel imaging at 6.5 mT, and is fully equipped for Overhauser DNP experiments. We continue to improve the ability to acquire images based on the intrinsic ¹H signal by combining new low-field hardware methodology and advanced pulse sequence and reconstruction methods.

Our second low field imaging test bed, the permanent magnet Halbach LFI is based around a lightweight (45 kg) and portable magnet with a built-in encoding field for MRI. It is a highly specialized and potentially disruptive scanner that could greatly ease both the cost and burden of a field-forward instrument purpose-built for TBI imaging. The 2D imaging results acquired in the highly inhomogeneous magnetic field of the Halbach scanner using simultaneous NMR measurement to track magnet drift, and multi-channel receive arrays to unwrap image aliasing, and are encouraging. A truly portable MR system based on this technology has the potential to quickly detect brain injury at the site of injury, for instance in an ambulance prior to transportation to the hospital.

We have also been developing technology for a wholly new approach to brain imaging that may revolutionize the use of MRI for the assessment and treatment of secondary brain injury following TBI: direct tomographic detection of endogenous free radicals as an early marker for TBI. This new form of contrast, “injury-sensitive MRI”, is based on the enormous signal enhancement attainable with Overhauser DNP, converting the electron spin of endogenous free radicals into nuclear polarization using the Overhauser effect and subsequently imaging that modified nuclear polarization using low-field MRI (OMRI).

The imaging experiments presented above in the optimized electromagnet LFI are compelling: high quality ^1H brain MRI at 6.5 mT is in fact attainable over reasonable averaging times using high performance hardware and advanced MRI sequences. A critical question for this work is the understanding of the clinical balance and impact that the tradeoff between acquisition time and resolution implicit in imaging plays on the operation of a deployable scanner.

The low-field OMRI results presented above demonstrate promise for high-speed high-resolution free-radical imaging, and offers new perspectives for the measurement of free radicals in living organisms. The long-term goal of this work is an *in vivo* implementation of this technique. Free-radical sensitive low-field OMRI as a novel imaging and diagnostic MRI-based method with specificity to secondary-injury has the potential to clarify the mechanisms involved in secondary damage and the local effects of novel therapies. Time-critical imaging of free radicals can provide the unique interventional access critically needed for drug therapies and this technique would fill the clear need for an “injury imager”, suitable for non-invasive tomographic measurement (Figure 16).

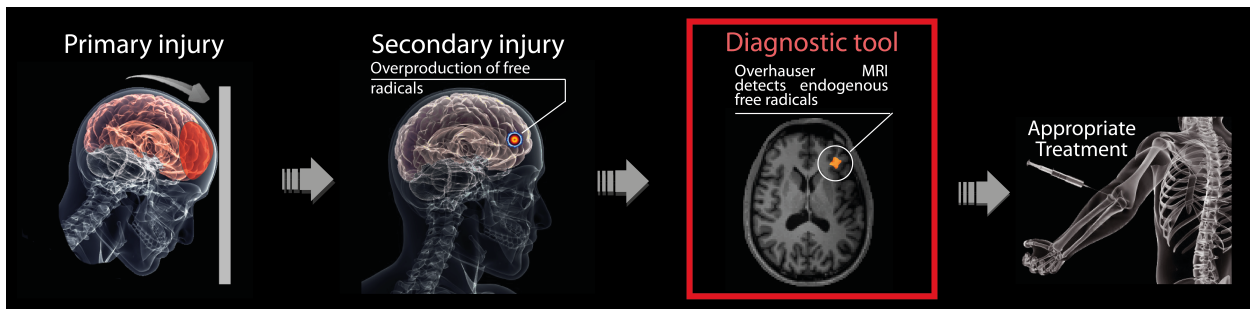


Figure 16: Schematic of the development of a new interventional imaging and treatment tool for *in vivo* detection of endogenous free radicals associated with secondary injury following TBI using low-field OMRI as developed here. This same approach can similarly open up new treatment windows into stroke and other ischemic events. MRI-based *in vivo* free radical imaging using OMRI is impossible at high-field due to the inability of the ESR pulse to penetrate into tissue, and the danger of RF heating in the microwave regime.

Successful demonstration of this system *in vivo* will provide image-based injury specificity for TBI and for the first time open a window into a critical mechanism of TBI-related disease and an unambiguous non-invasive *in vivo* marker for cerebral injury. Time-critical imaging of free radicals associated with secondary imaging can provide the unique interventional access critically needed to develop and deliver drug therapies to mitigate brain damage, reducing disability and death from secondary injury following TBI. The low-field approach would allow placement of this critical new diagnostic “injury imager” tool close to the source of injury—as well as in hospitals and clinics where rehabilitation takes place.

REFERENCES:

- [1] C. Z. Cooley, J. P. Stockmann, B. D. Armstrong, M. Sarracanie, M. H. Lev, M. S. Rosen, and L. L. Wald, "Two-dimensional imaging in a lightweight portable MRI scanner without gradient coils," *Magnetic Resonance in Medicine*, vol. 73, no. 2, pp. 872–883, Mar. 2014.
- [2] J. C. Sharp and S. B. King, "MRI using radiofrequency magnetic field phase gradients," *Magnetic Resonance in Medicine*, vol. 63, no. 1, pp. 151–161, Jan. 2010.
- [3] J. C. Sharp, S. B. King, Q. Deng, V. Volotovskyy, and B. Tomanek, "High-resolution MRI encoding using radiofrequency phase gradients," *NMR in Biomedicine*, vol. 26, no. 11, pp. 1602–1607, Jan. 2013.
- [4] H. M. Borsboom, T. Claasen-Vujčić, H. J. Gaykema, and T. Mehlkopf, "Low-frequency quadrature mode birdcage resonator," *Magnetic Resonance Materials in Physics, Biology and Medicine*, vol. 5, no. 1, pp. 33–37, 1997.
- [5] L. B. Casabianca, D. Mohr, S. Mandal, Y.-Q. Song, and L. Frydman, "Chirped CPMG for well-logging NMR applications," *Journal of Magnetic Resonance*, vol. 242, no. 0, pp. 197–202.
- [6] J. C. Sharp, D. Yin, B. Tomanek, and S. B. King, "Point-Spread-Functions for RF Imaging with TRASE: Implications for Phase Gradient Coil Design and Flip Angle Calibration," presented at the Proc. Intl. Soc. Magn. Reson. Med, Stockholm, Sweden, 2010, p. 1469.
- [7] L. A. O'Dell, "The WURST kind of pulses in solid-state NMR," *Solid State Nuclear Magnetic Resonance*, vol. 55, no. 0, pp. 28–41, Oct. 2013.
- [8] D. Kunz, "Frequency-modulated radiofrequency pulses in spin-echo and stimulated-echo experiments," *Magnetic Resonance in Medicine*, vol. 4, no. 2, pp. 129–136, Feb. 1987.
- [9] S. Ito and Y. Yamada, "Alias-free image reconstruction using Fresnel transform in the phase-scrambling Fourier imaging technique," *Magnetic Resonance in Medicine*, vol. 60, no. 2, pp. 422–430, Aug. 2008.
- [10] J. Hennig, A. M. Welz, G. Schultz, J. Korvink, Z. Liu, O. Speck, and M. Zaitsev, "Parallel imaging in non-bijective, curvilinear magnetic field gradients: a concept study," *MAGMA*, vol. 21, no. 1, pp. 5–14, Feb. 2008.
- [11] C. D. LaPierre, M. Sarracanie, L. L. Wald, and M. S. Rosen, "Parallel imaging and acceleration in the Johnson noise dominated regime," presented at the Proc. Intl. Soc. Mag. Reson. Med., Salt Lake City, UT, 2013, p. 2772.
- [12] C. D. LaPierre, L. L. Wald, and M. S. Rosen, "An Optimized 8-Channel Helmet Array for Head Imaging at 6.5 mT," presented at the Proc. Intl. Soc. Mag. Reson. Med. 19 (2011), Milan, Italy, 2014, p. 1325.
- [13] M. D. Harpen, "The spherical birdcage resonator," *Journal of Magnetic Resonance* (1969), vol. 94, no. 3, pp. 550–556, Oct. 1991.
- [14] J. E. Everett and J. E. Osemeikhian, "Spherical coils for uniform magnetic fields," *J. Sci. Instrum.*, vol. 43, no. 7, p. 470, 1966.
- [15] K. Golman, J. S. Petersson, J.-H. Ardenkjær-Larsen, I. Leunbach, L.-G. Wistrand, G. Ehnholm, and K. Liu, "Dynamic in vivo oxymetry using overhauser enhanced MR imag-

- ing,” *Journal of Magnetic Resonance Imaging*, vol. 12, no. 6, pp. 929–938, 2000.
- [16] H. Utsumi, K. Yamada, K. Ichikawa, K. Sakai, Y. Kinoshita, S. Matsumoto, and M. Nagai, “Simultaneous molecular imaging of redox reactions monitored by Overhauser-enhanced MRI with 14N-and 15N-labeled nitroxyl radicals,” *Proceedings of the National Academy of Sciences of the United States of America*, vol. 103, no. 5, p. 1463, 2006.
- [17] M. J. Ahn, E. R. Sherwood, D. S. Prough, C. Yie Lin, and D. S. DeWitt, “The effects of traumatic brain injury on cerebral blood flow and brain tissue nitric oxide levels and cytokine expression,” *Journal of Neurotrauma*, vol. 21, no. 10, pp. 1431–1442, 2004.
- [18] X. Zheng, K. Liu, and Y. Yang, “Real-Time Measurement of Murine HippocampusHippocampus NO Levels in Response to Cerebral Ischemia/ReperfusionReperfusion,” in Nitric oxide methods and protocols, vol. 704, no. 6, Totowa, NJ: Humana Press, 2010, pp. 73–80.
- [19] T. Malinski, F. Bailey, Z. G. Zhang, and M. Chopp, “Nitric oxide measured by a porphyrinic microsensor in rat brain after transient middle cerebral artery occlusion,” *Journal of Cerebral Blood Flow & Metabolism*, vol. 13, no. 3, pp. 355–358, 1993.
- [20] C. Iadecola, “Bright and dark sides of nitric oxide in ischemic brain injury,” *Trends in neurosciences*, vol. 20, no. 3, pp. 132–139, 1997.
- [21] L. Cherian, J. C. Goodman, and C. S. Robertson, “Brain nitric oxide changes after controlled cortical impact injury in rats,” *Journal of neurophysiology*, vol. 83, no. 4, pp. 2171–2178, 2000.
- [22] L. Cherian, J. C. Goodman, and C. Robertson, “Neuroprotection with Erythropoietin Administration Following Controlled Cortical Impact Injury in Rats,” *Journal of Pharmacology and Experimental Therapeutics*, vol. 322, no. 2, pp. 789–794, May 2007.
- [23] P. A. Rashid, A. Whitehurst, N. Lawson, and P. M. W. Bath, “Plasma nitric oxide (nitrate/nitrite) levels in acute stroke and their relationship with severity and outcome,” *Journal of Stroke and Cerebrovascular Diseases*, vol. 12, no. 2, pp. 82–87, Mar. 2003.
- [24] K. L. Carpenter, I. Timofeev, P. G. Al-Rawi, D. K. Menon, J. D. Pickard, and P. J. Hutchinson, “Nitric oxide in acute brain injury: a pilot study of NO(x) concentrations in human brain microdialysates and their relationship with energy metabolism.,” vol. 102, pp. 207–13, Jan. 2008.
- [25] M. Sarracanie, B. D. Armstrong, J. Stockmann, and M. S. Rosen, “High speed 3D overhauser-enhanced MRI using combined b-SSFP and compressed sensing,” *Magnetic Resonance in Medicine*, vol. 71, no. 2, pp. 735–745, Feb. 2014.
- [26] J. Mispelter, M. Lupu, and A. Briguet, NMR probeheads for biophysical and biomedical experiments : theoretical principles & practical guidelines. London : Imperial College Press ; Hackensack, NJ : Distributed by World Scientific,, 2006.
- [27] M. S. Rosen, M. Sarracanie, B. D. Armstrong, F. Herisson, N. Salameh, and C. Ayata, “Overhauser-enhanced MRI as a non invasive probe of BBB breakdown and redox state following ischemia/reperfusion,” presented at the Proc. Intl. Soc. Mag. Reson. Med., Milan, Italy, 2014, vol. 22, p. 6461.
- [28] E. Baudin, K. Safiullin, S. W. Morgan, and P. J. Nacher, “An active feedback scheme for low field NMR experiments,” *J. Phys.: Conf. Ser.*, vol. 294, p. 012009, Jun. 2011.

APPENDICES:

Year 4 Statement of Work:

We attach for reference the SOW for the No Cost Extension of Y4 as **Appendix 1**.

Abstracts accepted for presentation:

We attach seven abstracts (**Appendices 2–8**) accepted for presentation in 2015 that result from research presently funded in the Rosen lab by DoD/DMRDP. Abstracts marked with a ‡ will be presented as a poster at the 56th Experimental NMR Conference (ENC) to take place 20–24 May 2015 in Pacific Grove, CA, and abstracts marked with a § will be presented as a poster at the 24th Annual Meeting of the International Society for Magnetic Resonance in Medicine (ISMRM) to take place 1–5 June 2015 in Toronto, Canada. A symbol printed in red indicates that the abstract will be presented as a talk.

1. ‡§ 3D Balanced-EPI Magnetic Resonance Fingerprinting at 6.5 mT
2. ‡§ Low Cost High Performance MRI
3. ‡§ Dynamic in vivo free radical imaging with Overhauser-enhanced MRI
4. ‡§ 3D Imaging in a Portable MRI Scanner using Rotating Spatial Encoding Magnetic Fields and Transmit Array Spatial Encoding (TRASE)
5. ‡§ High Performance Probe for in vivo Overhauser MRI
6. ‡§ A single channel spiral volume coil for in vivo imaging of the whole human brain at 6.5 mT
7. § Transmit Array Spatial Encoding (TRASE) with broadband WURST pulses for robust spatial encoding in inhomogeneous B0 fields

Manuscripts published/accepted for publication:

We attach as **Appendix 9** our manuscript “2D imaging in a lightweight portable MRI scanner without gradient coils”, published in *Magnetic Resonance in Medicine* in 2014.

HARVARD UNIVERSITY DEPARTMENT OF PHYSICS
17 OXFORD STREET
CAMBRIDGE, MASSACHUSETTS 02138

13 December 2013

Lance L. Nowell
Contract Specialist
Assistance Branch 4
U.S. Army Medical Research Acquisition Activity
Attn: MCMR-AAA-AD
820 Chandler Street
Fort Detrick, MD 21702-5014

RE: NCE Request for ARO DMRDP Award # W81XWH-11-2-0076

Per you email request of Tues December 12 please find the following information in support of my EWOF request.

During the extension period, we will be completing the following tasks:

* Part of Task 1A: **Enable 3rd-axis (axial) encoding with Halbach permanent imager using TRASE coil.** This is a critical piece of technology needed to fully realize true 3D MRI in a portable lightweight (<100 lb) head imager, and is one of the two novel MRI scanners developed under this grant. This task been delayed because of technical issues surrounding RF power handling issues.

* Part of task 1C: **3. Test image-based free radical sensitivity of OMRI system.** We have identified Professor of Chemistry D. Whitney King (Colby College) as a collaborator on this task. His laboratory has developed a calibrated superoxide generator, which he will bring to the Rosen Laboratory at Harvard. We will use this instrument to directly investigate OMRI sensitivity to biologically relevant superoxide at nanomolar to micromolar concentrations. This is a critical step to understand the biological relevance and applicability of the new method of free radical imaging developed in the Rosen lab under this grant. This task had been delayed because more time then budgeted was spent improving detection strategies, as we continued to make gains in this regime.

Plan for use of unobligated funds:

This no-cost extension is requested because of technical delays in the current program. This request for a no cost extension will enable the previously approved objectives to be carried out. During the requested extension, the budget will be spent in accordance with the original budget and budget justification. No additional funds are requested.

With very best regards,



Matthew S. Rosen, Ph.D.

LOW-FIELD MRI AND HYPERPOLARIZED MEDIA LABORATORY
MGH/MARTINOS CENTER FOR BIOMEDICAL IMAGING
149 13TH STREET, SUITE 2301
CHARLESTOWN, MA 02129
LAB: 617 643 8636, FAX: 617-726-7993
martinos.org/lfi

Appendix 1: Year 4 NCE/Statement of Work

3D Balanced-EPI Magnetic Resonance Fingerprinting at 6.5 mTMathieu Sarracanie^{1,2}, Ouri Cohen¹, and Matthew S Rosen^{1,2}¹*MGH/A.A. Martinos Center for Biomedical Imaging, Charlestown, MA, United States;* ²*Department of Physics, Harvard University, Cambridge, MA, United States***Purpose**

In recent work [1], we demonstrated high speed MRI in the very low magnetic field regime (6.5 mT) using a balanced steady state based (b-SSFP) [2] acquisition scheme. b-SSFP provides the highest SNR per unit time [2] and image contrast depends on the ratio T_2/T_1 . At very low field, most species have T_2 relaxation times approaching T_1 , so b-SSFP images are essentially proton density (PD) weighted. In previous work [3] we have shown that 2D MR Fingerprinting [4] can be implemented at low magnetic field and provide simultaneous quantification of T_1 and T_2 as well as proton density and B_0 field maps. MRF at low magnetic field creates a rapid dynamic series of low signal to noise ratio (SNR) images where the magnitude of each voxel of each image changes at every time step. Generally, the TR and flip angle of each image in the time series is varied pseudorandomly [5]. Here, we demonstrate MRF in 3D at 6.5 mT, using an optimized set of 15 flip angles and repetition times (FA/TR), in a Cartesian acquisition of k -space with a new hybrid b-SSFP-EPI sequence.

Methods

The low field MRI scanner was previously described [5]. The imaging sequence is a hybrid multishot b-SSFP-EPI with an echo-train of 4 echoes (Fig. 1). The sequence was set with matrix size = $64 \times 64 \times 5$, corresponding voxel size = $(2.5 \times 3.5 \times 10)$ mm 3 , FOV = $(125 \times 175 \times 50)$ mm 3 , number of average NA = 2. The minimum TR was 62 ms with 9091 Hz bandwidth. The total acquisition time was 25 min. A flip (FA/TR) trajectory of length N=15 was generated using an optimization method previously described [6]. Lack of SNR at low magnetic field required redesigning our optimization scheme with a narrow range of larger flip angles [60-120°] and shorter TRs [62-400 ms]. The optimized FA/TR trajectory is compared to a non-optimized trajectory in Fig. 2. The imaged phantom consists in a stack of three 10 mm thick compartments of similar volume with different T_1 and T_2 properties.

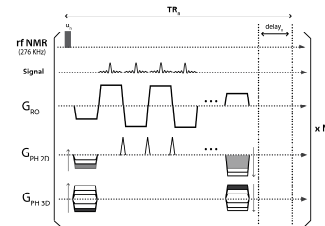


Figure 1: Pulse sequence diagram of the hybrid b-SSFP-EPI sequence used for 3D MR Fingerprinting. The FAs and TRs were set according to the optimized trajectory.

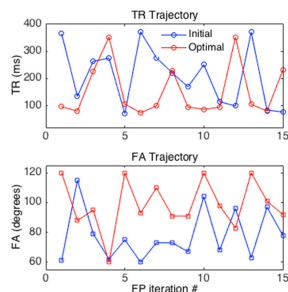


Figure 2: Comparison of our optimized trajectory with a random non-optimized trajectories for N=15.

Results

Each image generated in the reconstructed fingerprinting set (Figure 3) reveals different information. In regions with no signal (Slice 1, Slice 5), no matched value can be found. The spin density (M_0) map of Figure 3.a is equivalent to traditional b-SSFP, and only subtle differences are seen between compartments. Figure 3. b-c reveals that the compartment in slice 3 has the lowest T_1 and T_2 values, and that the compartment in slice 4 has the highest T_1 and T_2 values. Mean T_1 values are 200ms, 168ms, and 320 ms in slices 2, 3, and 4 respectively. Mean T_2 values are 180, 157, and 260 ms in slices 2, 3, and 4 respectively.

Conclusion

We have demonstrated 3D MR Fingerprinting at very low magnetic field with a hybrid b-SSFP-EPI sequence enabling fast and robust acquisition of k -space. The optimized FA/TR strategy provides good dispersion while drastically reducing the total acquisition time. We measure quantitative parameters in 3D, and generate several image contrasts in a single acquisition (proton density, T_1 , T_2) in less than 30 minutes. This technique is of particular relevance at low magnetic field where SNR and contrast are tied to long acquisition times. The combination of 3D MRF with low field MRI scanners has great potential to provide clinically relevant contrast with portable low cost MR scanners.

References: [1] Sarracanie M *et al.* Proc. ISMRM 2013 #5322; [2] Scheffler K *et al.* Eur Radiol 2003 13:2409-18; [3] Sarracanie M *et al.* Proc. ISMRM 2014 #6370; [4] Ma D *et al.* Nature 2013 495:187-193; [5] Tsai LL *et al.* JMR 2008; 193:174-85; [6] Cohen *et al.* Proc ISMRM 2014 #7153

Acknowledgement: This research was supported by the Department of Defense, Defense Medical Research and Development Program, Applied Research and Advanced Technology Development Award W81XWH-11-2-0076 (DM09094).

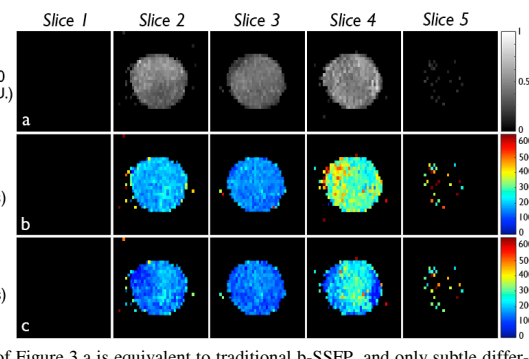


Figure 3 : MR Fingerprinting results at 6.5 mT : a. M_0 , b. T_1 , and c. T_2 in 3D, in a 3 compartment phantom. Each slice in the figure matches one of the phantom compartments.

Low Cost High Performance MRI

Mathieu Sarracanie^{1,2}, Cristen LaPierre^{1,2}, Najat Salameh^{1,3}, David E J Waddington^{1,3}, Thomas Witzel¹, and Matthew S Rosen^{1,2}
¹MGH/A.A. Martinos Center for Biomedical Imaging, Charlestown, MA, United States, ²Department of Physics, Harvard University, Cambridge, MA, United States,
³ARC Centre of Excellence for Engineered Quantum Systems, School of Physics, University of Sydney, Sydney, NSW, Australia

Purpose

Magnetic Resonance Imaging (MRI) is unparalleled in its ability to non-invasively visualize anatomical structure and function with high spatial and temporal resolution and a broad range of clinically relevant contrasts. Yet to overcome the low sensitivity inherent in NMR-based detection, the vast majority of clinical scanners incorporate superconducting magnets operating at 1.5, 3 tesla (T), and more exceptionally at 7T. These powerful magnets are massive, costly to purchase and maintain, and operate with very strict infrastructure demands and siting requirements that preclude operation in many environments. For brain imaging, low-field alternatives have been developed that rely on superconducting quantum interference devices (SQUID) detector arrays combined with magnetic field cycling techniques [1-4]. To date, this approach is limited by prohibitively long acquisition times (> 1 hr) and restrictions on attainable fields of view. We demonstrate here 3D brain MRI *in vivo* at 6.5mT (more than 450 times lower than clinical MRI scanners) in 6 minutes, by combining a high performance single channel Tx/Rx coil with modern undersampling techniques and b-SSFP [5].



Figure 1 : 3D printed single channel volume head coil. The coil was used for both transmit and receive at 276 kHz (6.5 mT)

Methods

To minimize B_1 inhomogeneity and maximize filling factor, a close fitting single channel inductive head coil for operation at 276 kHz was designed and 3D printed (Fig. 1). The coil features a 30-turn 3D spiral with turn-to-turn distance of 5.6 mm, thus ensuring the B_1 field produced is everywhere orthogonal to the main magnetic field B_0 . The hemispheric spiral design results in a very homogeneous magnetic field [6,7] over the volume of interest, making it suitable for both RF transmit and receive. Litz wire was selected due to its lower AC resistance compared to solid copper wire, reducing the Johnson noise of the coil while maintaining the same inductance. Previously [8], we described our use of undersampling strategies to accelerate low-field imaging. We make use of this here by randomly sampling 50% of k-space using a variable density Gaussian pattern. Once reconstructed, the images were apodized and processed using Perona and Malik anisotropic diffusion filtering [9] (ADF).

Results

Three-dimensional undersampled images acquired in 6 minutes (NA=30) are shown in Fig. 2 for each of the three spatial orientations (axial, coronal, and sagittal). We obtain $2.5 \times 3.5 \times 8.5 \text{ mm}^3$, $2.5 \times 3.5 \times 14.4 \text{ mm}^3$, and $2.5 \times 3.5 \times 11.5 \text{ mm}^3$ voxel resolution images in axial, sagittal and coronal orientation, respectively. Images with NA=160 acquired at 6.5 mT are compared to b-SSFP images acquired at 3T in Fig. 3.

Conclusion

At 6.5 mT, (more than 450 times lower than clinical MRI scanners) we demonstrate $2.5 \times 3.5 \times 8.5 \text{ mm}^3$ resolution in the living human brain in 6 minutes. We contend that robust non-field-cycled low-field implementations of MRI (< 10 mT) have the potential to make clinically relevant images and set new standards for a completely new category of affordable and robust portable devices.

References:

- [1] Zotev *et al.* J. Magn. Res. 2008 194(1):115-120;
- [2] Espy *et al.* J. Magn. Res. 2012 228:1-15;
- [3] Vesanen *et al.* Magn. Reson. Med. 2012 69(6):1795-1804;
- [4] Inglis *et al.* PNAS 2013 110(48):19194-201;
- [5] Scheffler K *et al.* Eur Radiol 2003 13:2409-18;
- [6] Harpen J. Magn. Res. 1991 94(3):550-556;
- [7] Everett *et al.* J. Scientific Instruments 1966 43:470-474;
- [8] Sarracanie *et al.* Magn. Reson. Med. 2013 71:735-745;
- [9] Perona *et al.* 1990 IEEE Trans. Pattern Anal. Mach. Intell. 12(7):629-639.

Acknowledgement: This research was supported by the Department of Defense, Defense Medical Research and Development Program, Applied Research and Advanced Technology Development Award W81XWH-11-2-0076 (DM09094).

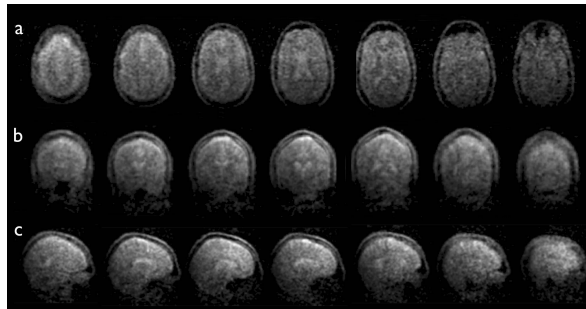


Figure 2: 3D images of the living brain (7 central slices of 15 slice dataset are shown) acquired in 6 minutes at 6.5 mT (276 kHz) in a. axial, b. coronal, and c. sagittal orientation. Acquisition matrix: $64 \times 75 \times 15$, Flip angle = 70° , BW = 9091 Hz, TR/TE = 23/11.7 ms, NA=30, voxel size: a. $(2.5 \times 3.5 \times 8.5) \text{ mm}^3$, b. $(2.5 \times 3.5 \times 11.5) \text{ mm}^3$, and c. $(2.5 \times 3.5 \times 14.4) \text{ mm}^3$.

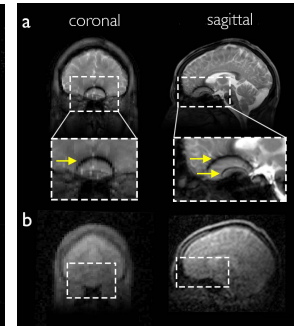


Figure 3: Comparison of b-SFFP images at a. 3T and b. 6.5 mT. Strong banding artifacts appear at high magnetic field (yellow arrows) whereas no artifact is seen in the images acquired at low field.

Dynamic *in vivo* free radical imaging with Overhauser-enhanced MRI

Mathieu Sarracanie^{1,2}, Fanny Herisson³, Najat Salameh^{1,2}, David E J Waddington^{1,4}, Cenk Ayata³, and Matthew S Rosen^{1,2}

¹*MGH/A.A. Martins Center for Biomedical Imaging, Charlestown, MA, United States*, ²*Department of Physics, Harvard University, Cambridge, MA, United States*, ³*Neurovascular Research Lab, Department of Radiology, Massachusetts General Hospital, Charlestown, United States*, ⁴*ARC Center for Engineered Quantum Systems, School of Physics, University of Sydney, Sydney, NSW, Australia*

PURPOSE: Free-radical-sensitive Overhauser-enhanced MRI (OMRI) is a promising technique for imaging the distribution and dynamics of free radicals, and a recently developed fast high-resolution OMRI methodology (1) offers new perspectives for the imaging of free radicals in living organisms. This method has been used to probe BBB breakdown following ischemic stroke in rats in conjunction with an injected stable free radical (2). Here we explore if OMRI can be used to acquire free radical images with sufficient spatial and temporal resolution to probe oxidative stress status in the brain. We present time-resolved *in vivo* measurements following single injection of TEMPOL. TEMPOL (4-hydroxy-TEMPO), a small molecule with a stable unpaired electron spin, is detected by OMRI with very high sensitivity. According to the literature, TEMPOL does not cross the BBB in a normal physiological state but does pass into brain parenchyma under pathological circumstances associated with oxidative stress and disease (3). As TEMPOL reduction has been used to non-invasively monitor tissue redox status in animal models (4), we hypothesize that time-resolved OMRI may be a tool to elucidating the redox status of brain tissue in neurologic diseases in which oxidative stress plays a significant role such as reperfusion injury (5), head trauma (6), Alzheimer's dementia (7) and multiple sclerosis (8).

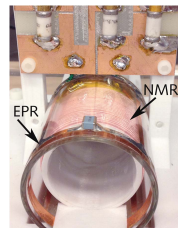


Figure 1: Probe for OMRI imaging at 6.5 mT: NMR: 276 kHz, ESR: 141 MHz.

METHODS: A custom built, low-field MRI scanner equipped with a biplanar 6.5 mT electromagnet and biplanar gradients was used in these experiments (9). 3D OMRI was performed using an optimized sequence based around b-SSFP as described in (1). *In vivo* experiments were performed using a modified Alderman-Grant ESR coil outside of a high sensitivity solenoid NMR coil wound from 5/39/42 Litz wire that fits the rat head (Figure 1). Under isoflurane anesthesia, the right carotid bifurcation of a male Sprague Dawley rat was dissected and the pterygopalatine artery ligated. Retrograde cannulation (Micro-Renathane MRE40, Braintree Scientific) of the right carotid bifurcation was performed through the external carotid artery. The catheter, filled with saline 0.9% with heparin 50U/ml, was then tunneled to the back of the animal and connected to the injection system. Oxygen saturation, temperature, and cardiac and respiratory rates were continuously monitored.

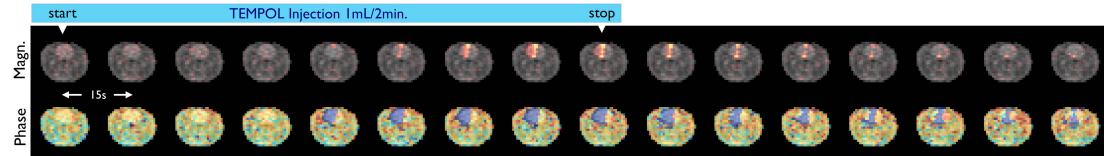


Figure 2: Dynamics of one slice from 3D OMRI dataset acquired from a rat at 6.5 mT: OMRI (color) magnitude and phase images (NA=1) are superimposed on anatomical MRI (grey), acquired in the OMRI scanner with DNP pulses disabled (NA=30). Anatomical imaging time was ~5 min. All images, voxel size $1.1 \times 1.6 \times 8 \text{ mm}^3$, TE/TR=25/50 ms, Matrix 128x35x11. TEMPOL (1.4 $\mu\text{l/gbw}$) was injected into the right ICA over 2 minutes.

Following acquisition of two reference scans (one with EPR off and one with EPR on), 1 ml of 150 mM TEMPOL was injected over 2 min with an infusion pump (GenieTouch Kent Scientific). OMRI imaging began at the same time as the infusion, and continued for 105 seconds after the injection was complete. A full 11 slice OMRI acquisition was acquired every 9 seconds, followed by a 6 second delay. This was repeated 16 times. Total imaging time was 240 s.

RESULTS: The internal carotid artery is responsible of the vascularization of its ipsilateral hemisphere via its terminal branches. The Circle of Willis enables some cross vascularization of one hemisphere from the contralateral side. Therefore, one would expect the cerebral distribution of a compound injected directly into the ICA to reflect the ipsilateral hemisphere and to a lesser degree the contralateral hemisphere. This is consistent with our dynamic *in vivo* OMRI results shown in Figure 2 and Figure 3, where marked DNP enhancement is seen in the hemisphere ipsilateral to the TEMPOL injection. As the Overhauser-enhanced signal has phase opposite to that of the thermal signal, the phase of the OMRI image in Figure 2 provides very sensitive contrast even in cases where the radical concentration is very low and the Overhauser enhancement may be small.

DISCUSSION & CONCLUSION: We have imaged the free radical TEMPOL with time-resolved OMRI methods *in vivo*. The use of fast bSSFP-OMRI in conjunction with an exogenously administered free radical molecule to probe redox status is a novel approach. As a method, temporally resolved OMRI may be used to study redox status of brain tissue made permeable to TEMPOL from oxidative stress. We note here that the long clearance times seen in some regions of the brain in Figure 2 may indicate TEMPOL in the brain parenchyma.

REFERENCES: (1) Sarracanie M et al. MRM 2014;71(2):735–45 ; (2) Rosen M S et al, Proc. ISMRM 2014 (22) 6461 ; (3) Behringer W et al. J Cereb Blood Flow Metab. 2002 22(1):105–17 ; (4) Hyodo F et al. J Pharm Pharmacol.2008 60(8):1049–60 ; (5) Chan PH. Stroke. 1996 27(6):1124–9 ; (6) Awasthi D, et al. Surg. Neuro. 1997 Jun;47(6):575–81 ; (7) Praticò D, et al Am. J. Med. 2000;109(7):577–85 ; (8) Fischer MT, et al Brain. Oxford Univ Press; 2012;135(3):886–99 ; (9) Tsai LL et al. JMR, 2008 93(2):274–85.

ACKNOWLEDGMENTS: This work supported by the Department of Defense, Defense Medical Research and Development Program, Applied Research and Advanced Technology Development Award W81XWH-11-2-0076 (DM09094).

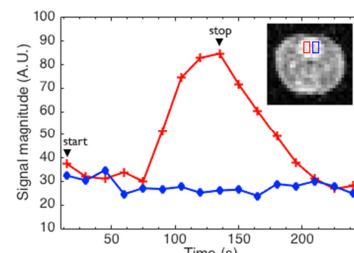


Figure 3: Mean OMRI magnitude from two brain ROIs: ipsilateral (red) and contralateral (blue) to the TEMPOL injection over the 240 s OMRI acquisition.

3D Imaging in a Portable MRI Scanner using Rotating Spatial Encoding Magnetic Fields and Transmit Array Spatial Encoding (TRASE)

Clarissa Zimmerman Cooley^{1,2}, Jason P Stockmann^{1,3}, Mathieu Sarracanie^{1,3}, Matthew S Rosen^{1,3}, and Lawrence L Wald^{1,2}

¹A. A. Martinos Center for Biomedical Imaging, Dept. of Radiology, Massachusetts General Hospital, Charlestown, MA, United States, ²Harvard Medical School, Boston, MA, United States, ³Dept. of Physics, Harvard University, Cambridge, MA, United States

PURPOSE: MRI could find wider applicability if low-cost, portable systems were available for siting in unconventional locations such as ICUs, physician offices, ambulances, or rural healthcare sites. The development of a previously described portable (<100kg) MRI scanner for brain imaging¹ is advanced with the implementation of 3rd axis encoding using the TRASE technique^{2,3}.

METHODS: Our 2D axial plane imaging without gradient coils utilized a rotating, 45 kg, 77 mT inhomogeneous Halbach cylinder based magnet¹. The built-in field variation of the permanent magnet array is used as a rotating spatial encoding magnetic field (rSEM). As the magnet is rotated around the sample, generalized projections onto the non-linear SEM are acquired as a spin-echo train.

To enable imaging in the 3rd direction (along the axis of the cylindrical magnet), we use the TRASE method. TRASE is a B_1^+ encoding method that requires 2 different switchable B_1^+ phase gradients (often equal and opposite) along the encoding direction^{2,3}. The 1D TRASE sequence (Fig. 2) is a modified RARE spin-echo train in which the slope of the B_1^+ phase gradient switches for consecutive refocusing pulses (indicated by the + or -). The 2 phase gradients correspond to 2 k-space origins ($-k_1$ and k_1), and the previous k-space point is flipped across the k-space origin of the refocusing pulse to traverse k-space.

Coils: A TRASE array was designed that consists of two nested cylindrical coils (Fig. 3). Coil 1 is a short 4-turn birdcage coil (12 rungs, 18cm diam., 22cm length)⁴ that produces a B_1^+ field in Y with a cosine shape along X, $B_{1y}^+(x) = |B_{1xy}^+| \cos(2\pi k_1 x)$. Coil 2 is a 10 turn Maxwell coil (22cm diam., 18cm length) that produces a B_1^+ field in X with a sine shape along X, $B_{1x}^+(x) = \pm |B_{1xy}^+| \sin(2\pi k_1 x)$. The coils are tuned to the Larmor frequency (3.29 MHz) and decoupled with a transformer (-20 dB isolation). Figure 3b, shows the relative magnitude of B_{1x} and B_{1y} from the 2 coils measured with a pick-up loop. When the two coils are driven with equal $|B_{1xy}^+|$ magnitude and spatial frequency, k_1 , they produce the desired B_1^+ field, $B_1^+(x) = |B_{1xy}^+| e^{+i2\pi k_1 x}$ (uniform magnitude and linear phase). A switchable 180° phase shifter is added in the Maxwell coil RF path, which applies a sign change to every other refocusing pulse. The pulses with the phase shift thus have a negative phase gradient; $B_1(x)^+ = |B_{1xy}^+| e^{-i2\pi k_1 x}$.

Acquisition: The 2D rSEM method and TRASE are performed simultaneously for 3D imaging. The TRASE array must rotate with the magnet because the Y direction changes as the magnet rotates. For every magnet rotation, the projection onto the SEM is acquired as a TRASE-modulated 16-echo spin-echo train (each echo: readout = 196 pt, BW = 40 KHz, echo spacing = 9.7 ms). Data is acquired at 180 rotations of the magnet spaced 1° apart. Frequency-swept WURST pulses are used to achieve the same flip angle across the inhomogeneous field (BW = 25 KHz, [pw90, pw180] = [6,3] ms)⁵. The birdcage coil of the TRASE array is used as the receiver coil.

Reconstruction: Step one separates the echo train data along X to obtain 16 different YZ-datasets corresponding to each slice. For each of the 186 points in the readout window, the set of 16 points along the echo train populates a k-space vector (Fig. 2). The points are rearranged and FFT'ed to generate a 1D projection along X (Fig. 4). Only the k-space lines formed from the center points of the echos result in 1D projections that are not modulated by the B_0 SEM. This is repeated for the echo trains from each of the 181 magnet rotations. Step two reconstructs each set of 181 echoes (YZ-data) into a 2D image of the corresponding slice. The encoding matrix for each slice is calculated using 2D B_0 field maps and then iterative matrix inversion¹ is performed to separately obtain each 2D image.

RESULTS: Figure 4 shows experimental 3D imaging results using a 7.5cm thick phantom with 1.5 cm water-filled compartments spaced 3 cm apart in X. A 1D projection along X shows the water-filled compartments. Three slices are reconstructed from data at X = -3cm, 0cm, and 3cm using the corresponding 2D B_0 field maps.

DISCUSSION: The non-bijectivity of the SEMs results in image aliasing across the center. This is usually resolved using a surface coil array⁶, but as a first step, the birdcage coil of the array was used for a receiver coil and only the reduced FOV image is shown. The blurring in the image slice is due to a combination of the spatially varying resolution of the SEMs and systematic calibration errors in our model-based reconstruction.

CONCLUSION: We demonstrate proof-of-concept 3D images in an inhomogeneous 45 kg magnet without the use of the gradient coils. TRASE encoding along X is ideal because like our 2D method it uses spin-echo trains, and it prevents the need for a B_0 gradient coil and GPA, which would add weight, cost, and power requirements to the portable, low-cost system. Future work will extend this 3D imaging method using larger diameter magnets and coils with the goal of portable low-cost MRI brain imaging.

REFERENCES: (1) Cooley C, MRM 2014. (2) Sharp JC, MRM 2010. (3) Sharp JC, NMR in Biomed. 2013. (4) Borsboom H, Magn. Reson. Mater. Phys. 1997. (5) Casabianca LB, JMR 2014, (6) Hennig J, Magn. Reson. Mater. Phys., 2008.

ACKNOWLEDGMENTS: The authors thank Jonathon Sharp, Scott King, Michael Garwood, Soumyajit Mandal, and Zohaib Mahmood for their help and advice. Support by NIH R01EB018976, NIH T90DA022759/R90DA023427, DoD/USAMRAA W81XWH-11-2-0076 (DM09094)

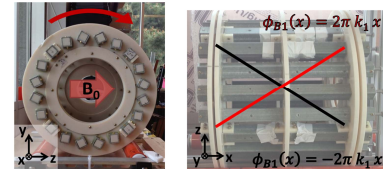


Figure 1: (a) Y-Z encoding is done with the rotating SEM method. (b) TRASE is done in the X direction using a switchable linear B_1^+ phase along X.

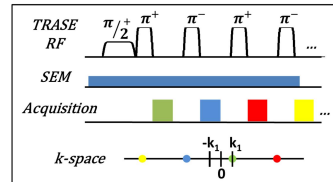


Figure 2: The TRASE sequence is repeated for every magnet rotation of the imaging sequence. The +/- indicates the sign of TRASE phase slope.

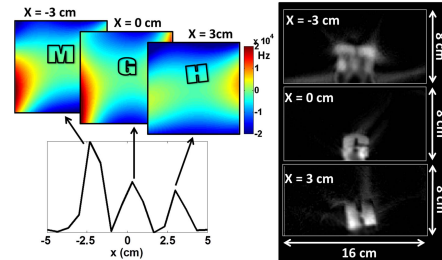
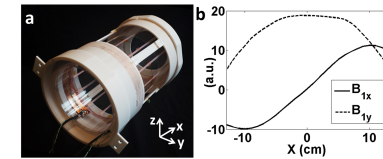


Figure 4: Image of a 3D phantom consisting of three water-filled compartments spaced 3 cm apart in X. A 1D projection along X for 1 rotation angle is shown (lower left). 3 image slices were reconstructed using the appropriate 2D field maps.

High Performance Probe for *in vivo* Overhauser MRI

David E J Waddington^{1,2}, Mathieu Sarracanie^{1,3}, Najat Salameh^{1,3}, and Matthew S Rosen^{1,3}

¹*MGH/A.A. Martinos Center for Biomedical Imaging, Charlestown, MA, United States*, ²*ARC Centre of Excellence for Engineered Quantum Systems, School of Physics, University of Sydney, Sydney, NSW, Australia*, ³*Department of Physics, Harvard University, Cambridge, MA, United States*

Purpose: Overhauser-enhanced MRI (OMRI) is an electron-proton double resonance imaging technique of much interest due to its ability to detect the concentration and distribution of free radicals. Tracking of exogenous free radicals with OMRI *in vivo* has enabled the development of oxymetry probes [1] and the imaging of redox reactions [2]. The large gyromagnetic ratio of electrons (28 GHz/T) demands that *in vivo* OMRI is performed at very low magnetic fields (~ 10 mT) in order to minimize RF heating and penetration depth issues. Operation at low magnetic field causes a drastic reduction in NMR sensitivity despite the signal enhancement that comes from the Overhauser effect, and emphasizes the need for high S/N probes. OMRI probe design is still relatively unexplored, despite its importance, and presents challenges unique to the frequencies of operation ($f_H = 276$ kHz and $f_e = 140.8$ MHz in our experiments at 6.5 mT). Here, we report the development of a high performance OMRI probe built to image free radical probes of the blood brain barrier following ischemic stroke in a rat model [3].

Methods: Our OMRI probe, consisting of an NMR solenoid inside a modified Alderman-Grant Resonator (Figure 1), was designed for use with a custom built, very low-field MRI scanner operating at 6.5 mT ($f_H = 276$ kHz) [4]. Images were acquired using a recently developed, fast, high-resolution b-SSFP based OMRI methodology [5]. NMR probe design in the low-field regime is fundamentally different to that at conventional MRI fields as thermal noise due to the intrinsic resistance of the pickup coil dominates over sample noise. This leads to a compromise where S/N improvements come at the expense of imaging bandwidth $S/N \sim \sqrt{Q} \sim 1/\sqrt{BW}$. An 85 turn solenoid was wound, using low AC resistance 5/39/42 litz wire, on a 3D printed polycarbonate former. This high filling factor coil has a bandwidth of 3 kHz.

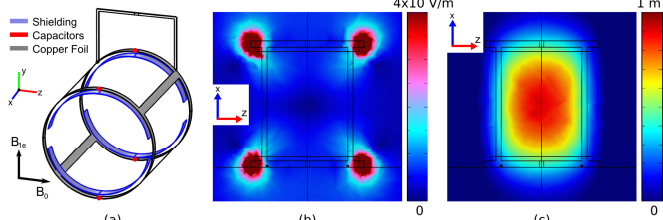


Figure 2: COMSOL Multiphysics simulations (a) Our modified Alderman-Grant Resonator. (b) Plot of $|E|$ showing that the electric field is strongly suppressed inside the resonator. (c) B_{1e} shows high homogeneity in the imaging volume – less than 10% variation across the imaging region.

TEMPOL (4-hydroxy-TEMPO) a stable radical, is detected by OMRI with high sensitivity, and because of its small size may facilitate imaging blood brain barrier leakage in cases of oxidative stress [3]. Simulations were validated in 2mM TEMPOL solutions (not shown) using simple spectroscopic measurements as well as fast imaging strategies [5]. The ESR resonator was tuned to 141 MHz, the lowest frequency of the TEMPOL triplet state at 6.5 mT, to minimize RF heating during ESR irradiation.

Results: Previously we reported the development of an OMRI probe for a rat head model utilizing an NMR solenoid and ESR surface coil [3]. Testing of our new OMRI probe shows that it has 3x the S/N of the probe reported in [3] and rectifies problems with B_{1e} homogeneity, yielding homogeneous enhancement of ~ -6.7 in 2mM TEMPO when 10 W of RF power is applied.

In vivo OMRI signal enhancement is clearly visible in the rat brain after TEMPOL injection, as shown in Figure 3. As the Overhauser-enhanced signal has a phase opposite to that of the thermal signal, the phase image in Figure 3 provides sensitive contrast in regions of low TEMPOL concentration.

Discussion and Conclusion: We have implemented a high performance probe for high temporal and spatial resolution OMRI in a rat brain. The S/N of this probe may be further improved, whilst maintaining imaging bandwidth, by using an active feedback circuit [7]. Higher S/N could also be realized through supercooling of the NMR solenoid or by using a free radical with a longer T_{1e} such as triphenylmethyl [1]. This probe may allow the *in vivo* detection of rapid redox changes in pathologic tissues, specifically in the context of brain trauma or stroke.

References: [1] K. Golman *et al.*, *J. Mag. Res. Im.*, 12, 929-938 (2000). [2] Utsumi *et al.*, *PNAS*, 103, 1463-1468 (2006). [3] M. Rosen *et al.*, *ISMRM*, 6461 (2014). [4] Tsai *et al.*, *J. Mag. Res.*, 193, 274-285 (2008). [5] M. Sarracanie *et al.*, *Magn Res. Med.*, 71, 735-745 (2014). [6] Mispelter *et al.*, ‘NMR Probeheads: For Biophysical and Biomedical Experiments’, Imperial College (2006). [7] Baudin *et al.*, *J. of Phys. Conf. Series*, 294, 012009 (2011).

Acknowledgements: This research was supported by DOD DMRDP Award W81XWH-11-2-0076 (DM09094). DW was supported by ANSTO and the Australian-American Fulbright Commission. NS was supported by the Swiss National Science Foundation (P3000P2_147768).

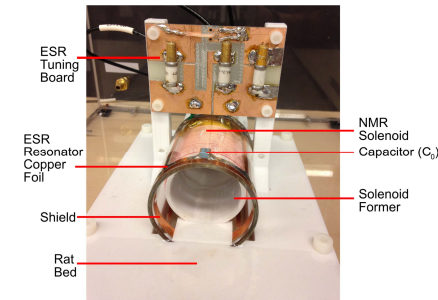


Figure 1: NMR/ESR rat head probe for operation at 6.5 mT. The ESR resonator is tuned to 140.8 MHz. The litz wire NMR solenoid coil (276 kHz) resonator board is not shown.

A modified Alderman-Grant ESR resonator was built using copper foil on Pyrex tubing. All metal placed in close proximity to the NMR solenoid strongly couples, reducing the NMR sensitivity. We therefore minimized amount of copper in the ESR resonator. Windows were removed from the panels on the sides of an Alderman-Grant resonator, a region of low current flow [6], in an attempt to reduce coupling whilst maintaining B_1 homogeneity. Shielding at the ends of the resonator prevents high electric fields at the capacitors penetrating the imaging volume, important because $P_{RF\text{-absorbed}} \sim E^2$. Slits in the shielding prevent the formation of closed loops that couple to the solenoid. Figure 2 demonstrates the high B_1 homogeneity and strong E suppression in our ESR resonator.

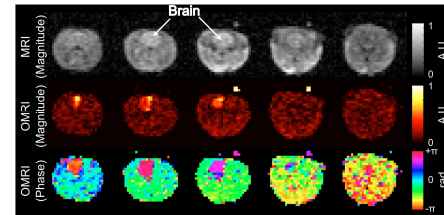


Figure 3: OMRI images acquired from a rat at 6.5 mT following injection of 1mL of 150 mM TEMPOL. Five slices from an 11 slice data set shown. OMRI (NA=1) imaging time was 9 seconds. Anatomical MRI (NA=30) was acquired in the OMRI scanner with ESR power disabled. All images, voxel size: 1.1 x 1.6 x 8 mm³, Matrix: 128 x 35 x 11

A single channel spiral volume coil for in vivo imaging of the whole human brain at 6.5 mT

Cristen LaPierre^{1,2}, Mathieu Sarracanie^{1,2}, David E J Waddington^{1,3}, and Matthew S Rosen^{1,2}

¹MGH/A.A. Martinos Center for Biomedical Imaging, Charlestown, MA, United States, ²Department of Physics, Harvard University, Cambridge, MA, United States,

³ARC Centre of Excellence for Engineered Quantum Systems, School of Physics, University of Sydney, Sydney, NSW, Australia

Purpose: MRI at low magnetic field (<10 mT) without cryogenic or hyperpolarization techniques presents unique engineering challenges. Imaging coils must maximize coverage over the volume of interest while minimizing losses in a regime unusual in contemporary MRI—where Johnson noise dominates the noise floor. Our previous work validated our scanner hardware and pulse sequences MRI at 6.5 mT. The purpose of the present work is to construct a high-performance coil for low-field imaging of the human brain *in vivo*.

Methods: Our previous coils focused on implementing array coil technology common at clinical field strengths, and we constructed an 8 channel receive-only coil for our 6.5 mT low-field imager at 276 kHz. While our results were promising^{1,2}, a lack of low noise high-impedance pre-amplifiers at our frequency regime prevented us from achieving sufficient coil decoupling, resulting in images with poor SNR. We present here a single channel coil with greatly improved SNR for these applications.



Figure 1: Form fitting helmet with 30-turn spiral design.

Results: From simulations, we built a 30-turn spiral wound with Type 1 40/38 Litz wire. Our aligned turn-to-turn spacing was 5.6 mm. The final design was 3D printed using fused deposition modeling technology with polycarbonate in a Fortus 360 mc printer (Stratasys, Eden Prairie, MN, USA), (Figure 1).

Images were acquired at 6.5 mT in a head shaped phantom using 3D b-SSFP with 50% undersampling. Resulting voxel size was $3.9 \times 3.5 \times 16.7 \text{ mm}^3$ (NA=110) (Figure 2a). A maximum in-plane SNR of 130 was calculated. An image of a similar slice obtained with the 8-channel array coil is shown for comparison (Figure 2b, combined image using RSS, voxel size = $4.4 \times 4.2 \times 22 \text{ mm}^3$, NA = 80, max SNR = 16.5).

19 slices of structured resolution phantom imaged with optimized spiral volume coil are shown in Figure 3. This four-quadrant phantom is filled with liquid-filled spheres of various diameters. Voxel size in this scan is $3.5 \times 2.5 \times 5 \text{ mm}^3$ with NA=40 and maximum SNR of 24.8. Total acquisition time is 10 minutes.

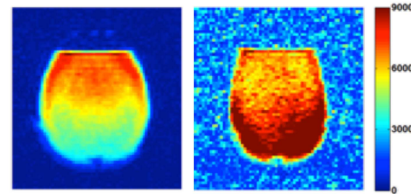


Figure 2: Equivalent slices in a head phantom acquired using the single channel spiral coil (A) and the 8-channel array (B) at 6.5 mT. Images are scaled by their maximum intensity.

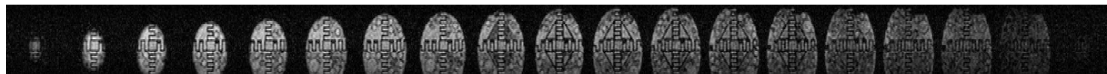


Figure 3: Axial view of a multi-compartment head-shaped phantom acquired with the Litz spiral volume coil at 6.5 mT in 10 minutes.

Discussion: A 30-turn single channel volume spiral coil designed for low field imaging significantly outperformed our 8-channel array coil. By minimizing losses in the coil, maximizing filling factor and eliminating coupling issues, we were able to obtain significantly higher SNR.

Conclusions: A high filling factor human-head Tx/Rx spiral volume imaging coil was successfully designed and constructed for 6.5 mT (276 kHz).

Financial Disclosure: This research was supported by the Department of Defense, Defense Medical Research and Development Program, Applied Research and Advanced Technology Development Award W81XWH-11-2-0076 (DM09094).

- References:**
1. LaPierre CD, et al. Proc. Intl. Soc. Mag. Reson. Med. 21 (2013) 2772
 2. LaPierre CD, et al. Proc. Intl. Soc. Mag. Reson. Med. 22 (2014) 1325
 3. Harpen MD. JJ Magn Res 1991;94(3):550–6.
 4. Everett JE and Osemeikhan JE. J. Sci. Instrum. 1966;43(7):470.

Transmit Array Spatial Encoding (TRASE) with broadband WURST pulses for robust spatial encoding in inhomogeneous B_0 fields

Jason P Stockmann^{1,2}, Clarissa Cooley^{3,4}, Mathieu Sarracanie^{1,2}, Matthew S Rosen^{1,2}, and Lawrence L Wald^{1,4}

¹A. A. Martinos Center for Biomedical Imaging, Massachusetts General Hospital, Charlestown, MA, United States, ²Department of Physics, Harvard University, Cambridge, MA, United States, ³Massachusetts General Hospital, Charlestown, MA, United States, ⁴Harvard Medical School, Boston, MA, United States

TARGET AUDIENCE: MRI engineers working with inhomogeneous B_0 fields

PURPOSE: Transmit array spatial encoding (TRASE)¹ uses RF coils with linearly-varying B_z^* phase to replace B_0 gradient phase encoding along one more directions. To traverse k-space, the sign of the B_z^* phase is flipped for alternating refocusing pulses in a spin echo train, imparting an additional Δk phase modulation to each successive echo in the train. TRASE provides an alternative for performing high resolution spatial encoding in applications where conventional B_0 gradients are not feasible. However, the TRASE point spread function degrades rapidly for refocusing pulse angles outside the range 150°–195° due to accumulation of flip angle and phase errors along the echo train². For the hard pulses (as shown in TRASE results to date), the refocusing angle falls below 150° when $\Delta B_0 > 40\%$ of the pulse Rabi frequency. This constrains the use of TRASE in applications where peak RF power is limited or ΔB_0 is large. We propose a method for overcoming this problem using broadband “WURST” RF pulses along with a simple deconvolution method to render the acquired echoes compatible with TRASE. **METHODS:** To demonstrate 1D TRASE in the presence of strong off-resonance, we acquire projections in an inhomogeneous Halbach array magnet (± 20 KHz over FOV) originally developed as a lightweight, permanent magnet-based portable MRI prototype³ with Larmor frequency 3.285 MHz (Fig. 1). WURST-40 pulses⁴ with phase cycling⁵ are used for spin excitation and refocusing. Pulses with linear frequency sweep impart a quadratic phase across the spin bandwidth, but if the pulse sweep rate satisfies the condition $R_{exc} = \frac{1}{2}R_{ref}$ and the ΔB_0 field is constant, then the refocusing pulse removes the phase applied by the excitation pulse and all isochromats refocus at TE . Further readouts in the echo train alternate between conventional echoes and “spectral” echoes⁵ that resemble the frequency distribution of spins in the ΔB_0 field. This additional RF phase modulation must be removed in order to make the spectral echoes compatible with TRASE. The spectral echo signal can be approximated as a convolution of the conventional spin echo signal with a chirp function, $\exp(i2\pi t^2)$, where t depends on the sweep rate. **DECONVOLUTION** is performed by either (a.) convolving the spectral echo with a scaled, conjugated version of the chirp function, or equivalently (b.) in the Fourier transform (FT) domain by dividing the FT of the echo (1D projection) by the FT of the chirp function⁷. Since the FT-ed chirp kernel is a pure phase term, method (b.) requires simply taking the difference between the phase of the first and second projections in the echo train (Fig. 2). This phase difference is used to correct all subsequent spectral echoes. The FT of the corrected spectral echoes yields echo magnitudes and phases that correspond closely to the conventional echoes in the train. **EXPERIMENT:** Tube phantoms are placed in the inhomogeneous B_0 field and a train of 129 echoes are acquired each with 196 readouts points, 40 KHz BW, and echo spacing 9.4ms. WURST-40 excitation and refocusing pulse durations are $[t_{exc}, t_{ref}] = [6, 3]$ ms and sweep rates are $[R_{exc}, R_{ref}] = [4.15, 8.3]$ MHz/s over a 25 KHz bandwidth. A multi-turn Maxwell coil (B_{1z}^*) is paired with a concentric multi-turn birdcage coil⁸ (B_{1y}^*) to generate sine and cosine-shaped B_z^* amplitudes, respectively, along the encoding axis, x . When both coils are driven simultaneously, the desired linear phase slope is generated: $B_{1tot}^+(x) = |B_{1xy}^+| \cos(2\pi kx) \pm i|B_{1xy}^+| \sin(2\pi kx) = |B_{1xy}^+| \exp(\pm i2\pi kx)$

The TRASE B_z^* phase is switched using an RF phase shifter to play the pattern: {90°, 180°, echo, 180°, echo, 180°, echo, 180°, ...}. The first two echoes have no TRASE modulation and can therefore be used to calculate the phase difference required for the spectral echo correction. To create a 1D projection along x , the point from the center of each readout is selected to avoid modulation imparted by the ΔB_0 field (Fig. 3). The points are reordered and FT-ed to create a 1D projection of the object. **RESULTS:** Fourier domain phase subtraction faithfully restores spectral echoes so that their real and imaginary components align closely with those of conventional echoes. The TRASE-WURST acquisition successfully generates projections of phantoms with bandwidths >10 KHz in the inhomogeneous B_0 field. By contrast, recognizable projections could not be obtained using hard pulse excitations since available RF power constrained the minimum pulse duration ([75, 150] μ s for [90°, 180°] pulses) and thus the bandwidth of the pulses. **CONCLUSION:** We demonstrate robust spatial encoding using WURST pulses for TRASE encoding in an inhomogeneous B_0 field. We further show a simple phase correction that allows WURST spectral echoes to be used for TRASE encoding. In future work, TRASE-WURST slice encoding will be combined with in-plane B_0 gradient encoding to generate 3D images. Potential applications include silent imaging, oil well prospecting, and portable low-field scanners. **REFERENCES:** [1] Sharp JC, NMR Bio. 2013. [2] Sharp JC, ISMRM 2010, p. 1469. [3] Cooley C, MRM 2014. [4] Kupce E, JMR 1995. [5] Casabianca LB, JMR 2014. [6] Kunz D, MRM 1987. [7] Ito S, MRM 2008. [8] Borsboom H, MAGMA 1997. **ACKNOWLEDGEMENTS:** The authors thank Jonathan Sharp, Scott King, and Soumyajit Mandal. Support from R01EB018976 and DoD/USAMRRA W81XWH-11-2-0076 (DM09094).

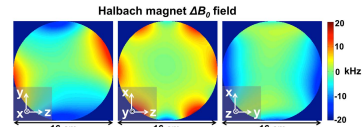


Fig. 1. Halbach magnet ΔB_0 field plotted along three planes. TRASE encoding is implemented along x direction.

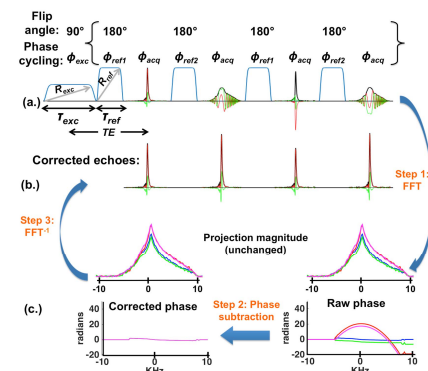


Fig. 2. WURST pulse sequence diagram with four echoes acquired on a water bottle phantom. The bracketed block is repeated as needed. Conventional echoes alternate with “spectral” echoes modulated by the quadratic phase of the frequency swept RF pulses. This effect is compensated by removing the quadratic phase from the projections corresponding to each spectral echo. After phase correction the echo real and imaginary parts overlay for all echoes in the train. Phase cycling scheme is as follows: $\phi_{exc} = [90, 270, 180, 0^\circ]$, $\phi_{ref1} = [0, 90, 90, 0^\circ]$, $\phi_{ref2} = [90, 90, 0, 0^\circ]$, $\phi_{acq} = [0, 180, 90, 270^\circ]$. The 3rd and 4th echoes in the block are multiplied by π to compensate for phase cycling.

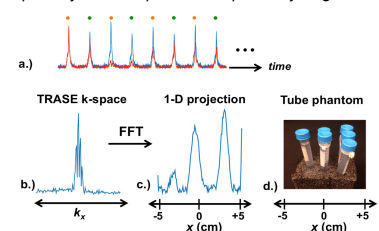


Fig. 3. The first 8 corrected echoes (a.) from a 128-echo train shown with (red) and without TRASE phase modulation. Orange and green dots at each echo time denote positive and negative k-space points, respectively, which are reordered into 1D k-space (b.). The Fourier transform yields a 128-point 1D projection (c.) of the water-filled tube phantom (d.).

Two-Dimensional Imaging in a Lightweight Portable MRI Scanner without Gradient Coils

Clarissa Zimmerman Cooley,^{1,2*} Jason P. Stockmann,^{1,3} Brandon D. Armstrong,^{1,3}
Mathieu Sarracanie,^{1,3} Michael H. Lev,^{4,5} Matthew S. Rosen,^{1,3,5}
and Lawrence L. Wald^{1,5,6}

Purpose: As the premiere modality for brain imaging, MRI could find wider applicability if lightweight, portable systems were available for siting in unconventional locations such as intensive care units, physician offices, surgical suites, ambulances, emergency rooms, sports facilities, or rural healthcare sites.

Methods: We construct and validate a truly portable (<100 kg) and silent proof-of-concept MRI scanner which replaces conventional gradient encoding with a rotating lightweight cryogen-free, low-field magnet. When rotated about the object, the inhomogeneous field pattern is used as a rotating spatial encoding magnetic field (rSEM) to create generalized projections which encode the iteratively reconstructed two-dimensional (2D) image. Multiple receive channels are used to disambiguate the nonbijective encoding field.

Results: The system is validated with experimental images of 2D test phantoms. Similar to other nonlinear field encoding schemes, the spatial resolution is position dependent with blurring in the center, but is shown to be likely sufficient for many medical applications.

Conclusion: The presented MRI scanner demonstrates the potential for portability by simultaneously relaxing the magnet homogeneity criteria and eliminating the gradient coil. This new architecture and encoding scheme shows convincing proof of concept images that are expected to be further improved with refinement of the calibration and methodology. *Magn Reson Med* 000:000–000, 2014. © 2014 Wiley Periodicals, Inc.

Key words: portable MRI; low-field MRI; nonlinear SEMs; Halbach magnet; parallel imaging

INTRODUCTION

Specialized, portable MRI systems have the potential to make MR neuroimaging possible at sites where it is currently unavailable and enable immediate, “point-of-care” detection and diagnosis of acute intracranial pathology which can be critical in patient management. For example, the characterization of acute posttraumatic space occupying brain hemorrhage is a time-sensitive emergency for which simple clinical assessment and even urgent computed tomography scanning may be insufficient. While conventional MR scanners are capable of making this diagnosis, they are not available in remote locations. In Intensive Care Units scanners are generally nearby, but are difficult to use because of the dangers associated with transporting critical care patients. A portable bed-side scanner could offer major benefits in such situations. Portable, low-cost scanners are compelling for applications where power, siting, and cost constraints prohibit conventional scanners. Examples include clinics in rural or underdeveloped areas, military field hospitals, sports arenas, and ambulances. Finally, analogous to the current use of ultra-sound, a low-cost and easy-to-implement scanner could find uses in neurology, neurosurgery, or neuro-oncology examination rooms for routine disease monitoring (e.g., monitoring ventricle size after stent placement). The development of a portable scanner relies on the co-design of a new image encoding methods and simplified hardware. This approach is detailed in the present work.

Traditional Fourier MR imaging methods rely on homogeneous static polarizing fields (B_0) and high strength linear spatial encoding magnetic fields (SEMs) produced by magnetic gradient coils. Conventional scanners use high cost superconducting wire, liquid cryogen cooling systems, and high power supplies and electronics. These aspects make it difficult to simply scale-down conventional MRI scanners to portable, low cost devices. Recently in Kose and Haishi (1) and Kimura et al (2), high resolution imaging has been achieved with tabletop and small bore permanent magnet systems with long acquisition times (1), including a mobile MRI system developed for outdoor imaging of small tree branches (2), but these scanners lack a bore size suitable for brain imaging and the long acquisition times are not conducive to imaging in triage settings. Other approaches that scale-down the size of conventional systems for intraoperative MRI show promise (3). However, while these systems are relatively easy to retrofit in operating room, they are not truly portable.

¹A.A. Martinos Center for Biomedical Imaging, Department of Radiology, Massachusetts General Hospital, Charlestown, Massachusetts, USA.

²Department of Electrical Engineering and Computer Science, Massachusetts Institute of Technology, Cambridge, Massachusetts, USA.

³Department of Physics, Harvard University, Cambridge, Massachusetts, USA.

⁴Department of Radiology, Massachusetts General Hospital, Boston, Massachusetts, USA.

⁵Harvard Medical School, Boston, Massachusetts, USA.

⁶Harvard-MIT Division of Health Sciences Technology, Cambridge, Massachusetts, USA.

Grant sponsor: The Department of Defense, Defense Medical Research and Development Program, Applied Research and Advanced Technology Development Award; Grant number: W81XWH-11-2-0076 (DM09094); Grant sponsor: NIH; Grant numbers: P41EB015896, T32DC00038; Grant sponsor: NIH Blueprint for Neuroscience Research; Grant number: T90DA022759/R90DA023427.

*Correspondence to: Clarissa Zimmerman Cooley, M.Eng., 149 13th Street, Room 2301, Charlestown, MA 02129. E-mail: czimmer@mit.edu

Additional Supporting Information may be found in the online version of this article.

Received 16 September 2013; revised 2 December 2013; accepted 5 January 2014

DOI 10.1002/mrm.25147

Published online 00 Month 2014 in Wiley Online Library (wileyonlinelibrary.com).

© 2014 Wiley Periodicals, Inc.

In the present work, we use a novel image encoding method based on rotating spatial encoding magnetic fields (rSEMs) to create a portable scanner. We replace the B_0 magnet and linear gradient coils with a rotating permanent magnet featuring an inhomogeneous field pattern used for spatial encoding. In this scheme, the inhomogeneity in the B_0 field serves as a spatial encoding magnetic field (SEM), and is requirement for image encoding not a nuisance. Loosening the homogeneity constraint of some conventional magnet designs leads to a reduction in the minimum required magnet material, and allows for more sparse/lightweight designs (45 kg in our prototype). Additionally, the rotation of the magnet's inhomogeneous field pattern replaces the function of heavy switchable gradient coils with significant power requirements.

Several NMR devices for niche applications have explored relaxing the magnet homogeneity constraint, as well as reducing the reliance on traditional Fourier image encoding. The oil well-logging industry was the first to explore the idea of mobile NMR using "external sample" or "inside-out" NMR tools for measuring fluid in rock formations down-hole (4). This work was initially done with electromagnets or in the earth's field, but the advent of rare-earth magnets with high energy products such as SmCo and NdFeB (5), has allowed more effective borehole NMR tools to be developed (6). Some portable single-sided NMR devices (7,8) exploit inhomogeneous magnetic fields from permanent magnets for 1D spatial encoding. In these systems a rare-earth magnet array is placed against the object such that the field falls off roughly linearly with depth. Broadband excitation and spin-echo refocusing are used to obtain a one-dimensional (1D) depth profile of the water content in the object (9–11). Thus, these systems use the inhomogeneity of the small magnet to spatially encode the depth of the water; a principle that we will exploit in a more complete way.

Previously, Cho et al implemented a mechanically rotating DC gradient field in conjunction with a conventional MRI scanner with the motivation of silent imaging (12). In that case, the rotating electromagnet produced a linear gradient field so traditional projection reconstruction methods could be used. In the presently described portable scanner, the dominant SEM field term is quadrupolar, which requires specialized acquisition and reconstruction techniques. Spatial encoding with similar nonlinear fields created with electromagnets has recently drawn attention as a way to achieve focused high imaging resolutions, reduced peripheral nerve stimulation (13), and improved parallel imaging performance (14). In our scanner, the approximately quadrupolar SEM fields are physically rotated around the object along with the B_0 field, and stationary RF coils are used to acquire generalized projections of the object in spin-echo train form.

In this manuscript, we describe the design, construction, and testing of a portable 2D MRI scanner. We show that the encoding scheme we introduce can achieve a resolution of a few millimeters in phantom images. While full 3D encoding is not demonstrated, the system is compatible with RF encoding schemes, such as the transmit array spatial encoding (TRASE) method (15,16),

capable of adequately encoding the third dimension (along the axis of the cylindrical magnet). The magnet design and initial encoding attempts were previously reported in abstract form (17–19).

METHODS

Magnet and Field Mapping

The described rSEM encoding method is valid for arbitrary encoding field shapes, although the shape will affect the spatially variable resolution of the images. A sparse dipolar Halbach cylinder design similar to the "NMR Mandhala" (20,21) was chosen to produce the rotating B_0 field presented here. This arrangement of permanent magnets produces an approximately uniform field directed transverse to the axis of the cylinder (22). The major design criteria for our Halbach magnet were: (i) maximum average field for highest signal to noise ratio (SNR), (ii) sufficient field variation for spatial encoding while maintaining reasonable measurement and excitation bandwidths, (iii) minimum volume of permanent magnet material to keep cost and weight down, (iv) use of stock rare-earth magnet material shapes, and (v) minimum size to fit the head (to maximize B_0). Note, the design was not focused on the specific spatial encoding field shape, and the resulting pattern in the constructed magnet was accepted as the SEM for the presented scanner. The Halbach cylinder design consists of a 36-cm-diameter array of 20 rungs comprising N42 grade NdFeB magnets that are each $1 \times 1 \times 14"$ (magnetized through the 1" thickness). Two additional Halbach rings made up of twenty 1" NdFeB cubes are added to the ends of the cylinder to reduce field fall-off caused by the relatively short length of cylinder. Figure 1 shows a 3D drawing of the magnet, the simulated field, and constructed magnet.

The predicted field pattern (Fig. 1a,b), as well as the forces between the magnet rungs were simulated using COMSOL Multiphysics (Stockholm, Sweden). This calculation estimated an internal force of 178 N, which is adequately handled by the fiberglass and ABS frame designed to hold the NdFeB magnet array. The magnet rungs consist of NdFeB magnets stacked inside square fiberglass tubes (McMaster-Carr, Elmhurst, IL, USA), which are fixed by five water jet cut 3/8"ABS rings (Fig. 1d). Each 14" long magnet rung is comprised of four individual bar magnets (Applied Magnet, Plano, TX, USA) which were bonded together (three 4" bars and a 2" bar). The ABS/fiberglass frame was assembled before NdFeB magnet handling, and then the magnet rungs were populated one at a time. Because the four magnets comprising each rung repel each other as they are inserted, a magnet loading and pushing jig was necessary to force the magnets together while the magnet bonding adhesive cured (Loctite p/n 331 and 7387, Düsseldorf, Germany). The jig was a simple threaded rod mounted to the magnet assembly frame above the opening of the fiberglass tube.

The constructed magnet weighs 45 kg and has a 77.3 mT average field in the 16-cm field of view (FOV) center plane, corresponding to a 3.29 MHz proton Larmor frequency. The cylindrical magnet sits on aluminum rollers

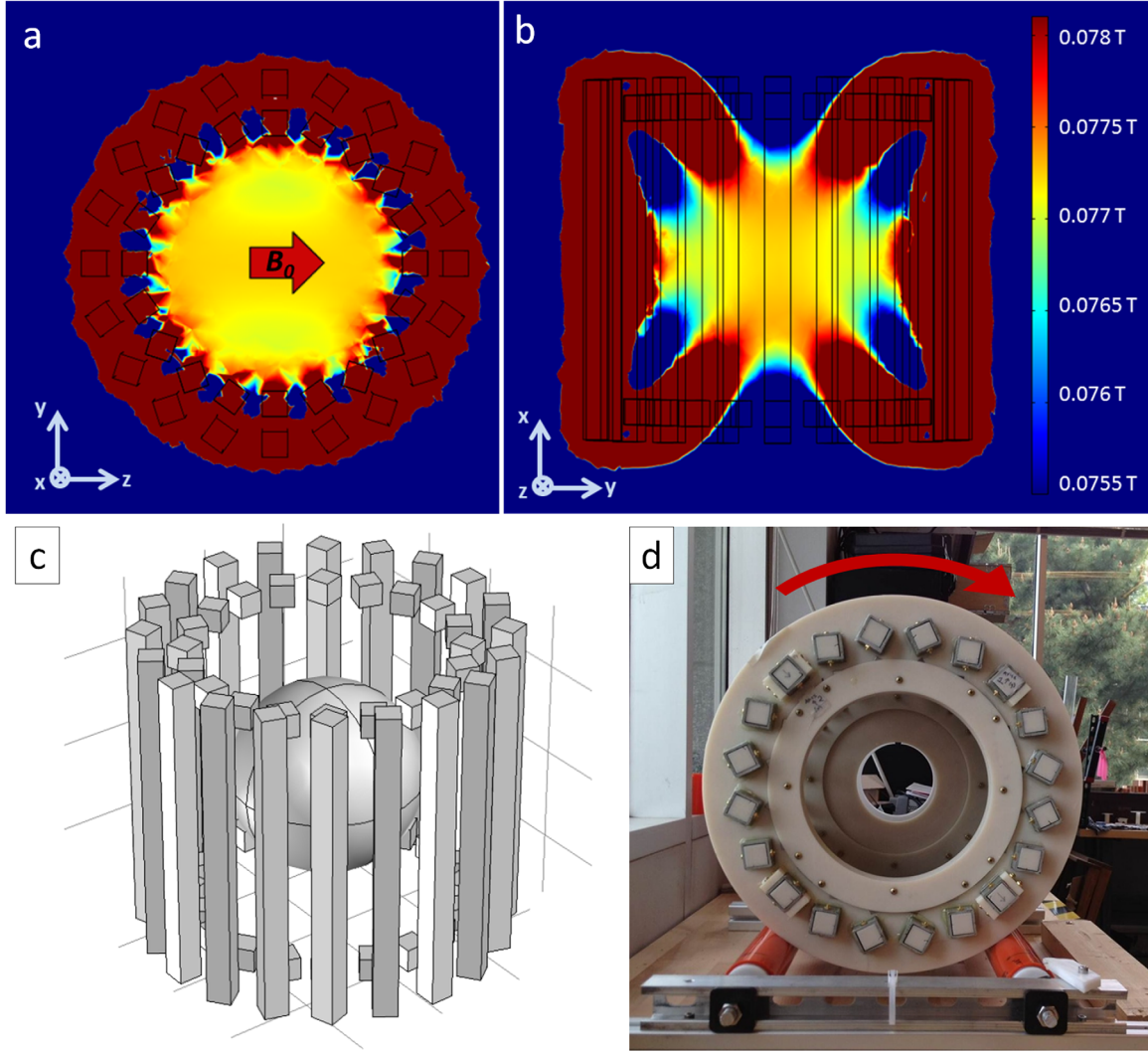


FIG. 1. The magnet array consists of twenty 1" × 1" × 14" NdFeB magnets oriented in the $k = 2$ Halbach mode. Additional Halbach rings made of 1" × 1" × 1" magnets were added at the ends to reduce field fall off along the cylindrical axis. **a,b:** Simulation of the magnetic field in two planes. The field is oriented transverse to the cylinder axis (z-direction). **c:** Schematic of NdFeB magnets composing array. The targeted spherical imaging region (18-cm diameter) is depicted at isocenter. **d:** End-view photo of the Halbach magnet mounted on high friction rollers. Magnet was constructed with ABS plastic and square fiberglass tubes containing the NdFeB magnets. Faraday cage not shown.

covered with a high friction urethane. The MRI console is used to drive a stepper motor (model 34Y106S-LW8, Anaheim Automation, Anaheim, CA, USA) that is attached to the aluminum axle of one of the rollers through a 5:1 gearbox (model GBPH-0901-NS-005, Anaheim Automation). Magnet rotation is incorporated into the pulse sequence so that it is controlled by the MRI console to a precision of one degree at a rate of 10 deg/s. Peripheral nerve stimulation is not a concern with this B_0 rotation rate. Even at 10 \times the current rotation rate, the dB/dt from the rotating magnet is two orders of magnitude below the dB/dt generated by a modest clinical gradient system. The magnet assembly is enclosed in a copper mesh Faraday cage to reduce RF interference.

An initial 3D field map was obtained with a three-axis gaussmeter probe attached to a motorized stage. The measured field shape is roughly quadrupolar, similar to the fields used in the initial realization of multipolar Pat-

Loc (Parallel Imaging Technique using Localized Gradients) encoding (13), but with significant higher-order components as well. The measured field variation range in y-z (imaging plane), x-z, and x-y planes of a 16-cm sphere were $\Delta f_{yz} = 95$ kHz, $\Delta f_{xz} = 60$ kHz and $\Delta f_{xy} = 52$ kHz. Large Larmor frequency bandwidths make it difficult to design RF excitation and refocusing pulses that achieve the same flip angle and phase across all the spins. In addition, it is difficult to make transmit and receive coils uniformly sensitive over the entire bandwidth. Therefore, shimming was done to decrease field variation (no attempt was made to reshape the SEM). The field variation was shimmed down to $\Delta f_{yz} = 32$ kHz, $\Delta f_{xz} = 32.5$ kHz and $\Delta f_{xy} = 19$ kHz with the addition of small shim magnets (0.5" diameter, 0.25" length cylindrical NdFeB magnets) which were attached to the fiberglass rungs. The three planes of the shimmed field map are shown in Figure 2.

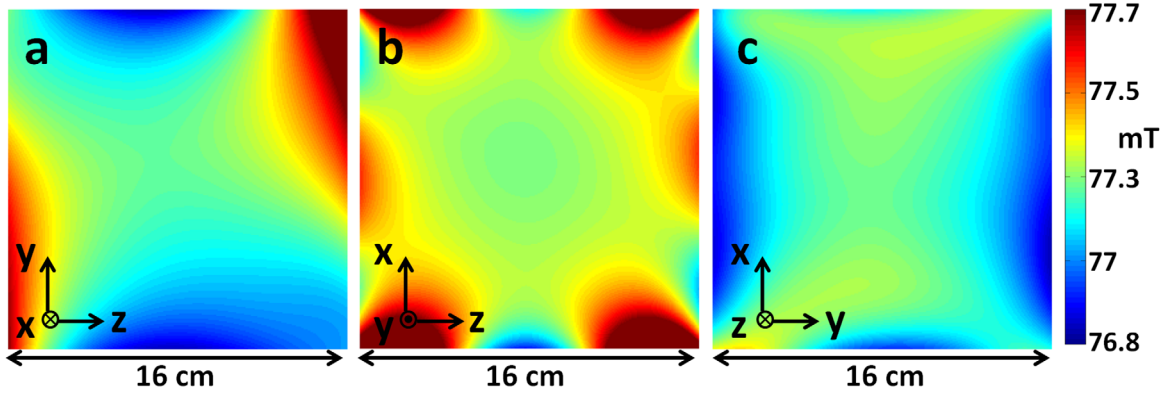


FIG. 2. Gaussmeter-measured field maps of the spatial encoding magnetic field (SEM) in the z-y (imaging plane), z-x, and y-x planes of shimmed the Halbach magnet. The B_0 field is oriented in the z direction.

An accurate field map is critical for image reconstruction, particularly when nonlinear encoding fields force the use of iterative matrix solvers rather than the Fourier transform (14). The field is perturbed by external fields (including the earth's magnetic field), and must be remapped when the magnet is relocated. To quickly acquire center-plane field maps, a linear array of seven field probes spaced 1.5 cm apart was constructed (Fig. 3a). The field probes are tuned 5-mm-long, 4-mm-diameter, 18-turn solenoids measuring signal from 1-mm capillaries of CuSO₄-doped water (23). To acquire a field map the probes are held stationary while the magnet is rotated around them. Polynomial basis functions are then fit to the measured points and the field map (Fig. 3b) is synthesized. The polynomial coefficients up to 6th order of one magnet rotation angle are shown in Table 1. The net magnetic field from the NdFeB magnets is sensitive to temperature (on the order of 4 kHz/deg C for the Halbach magnet) as well as interactions with external fields, so an additional field probe is used to monitor field drift during data acquisition. This navigator probe is mounted to the Halbach array and rotates with the magnet. The measured field changes, ΔB_0 , are then accounted for in the image reconstruction.

Acquisition Method

To acquire data, the magnet is physically rotated around the sample in discrete steps. At each rotation step, generalized projections onto the nonlinear field are acquired (similar to those described in Schultz et al) (24). Exam-

ples of these projections are shown in Figure 4 for a simple two-sphere phantom. The field experienced by the spheres changes at each rotation due to the nonlinear SEM, providing new information in each projection.

The constructed Rx coil array (Fig. 5a) consists of eight 8-cm-diameter loops of wire encircling the FOV on the surface of a 14-cm-diameter cylinder. The inductances of the coils are roughly 230 nH, requiring capacitors on the order of 10 nF (Voltronics, Salisbury, MD) for tuning. Geometric decoupling and PIN diode detuning were implemented (25,26). The coils are tuned and matched to 50 Ohm impedance low noise preamplifiers (MITEQ P/N AU-1583, Hauppauge, NY, USA).

A Tecmag Apollo console with TNMR software (Houston, TX, USA) was used. The console has one transmit channel, three gradient channels, and one receive channel. Because the programmable gradient analog outputs are not needed for gradient coils, they are used for other purposes. For example, the G_z gradient output is used to control the stepper motor for magnet rotation. The fact that the console only has 1 receive channel means that true parallel imaging cannot be performed. Instead, the receive channel is switched between the coils in the array, acquiring data serially. The G_x gradient output along with a RelComm Technologies (Salisbury, MD, USA) relay and Arduino UNO board are used to switch between the receive coils. Although preamp decoupling has not been implemented yet, data is being acquired from one coil at a time, permitting the other receive coils to be detuned to prevent coupling.

Two scanner coordinate systems are defined because the object and RF coils remain stationary while B_0 is

Table 1
Polynomial Composition of Halbach Magnet SEM in Hz/cm^(m+n)^a

z^ny^m	$n=0$	$n=1$	$n=2$	$n=3$	$n=4$	$n=5$	$n=6$
m=0	$z^0y^0 : 3.3e6$	$z^1y^0 : -89$	$z^2y^0 : -274$	$z^3y^0 : 1.9$	$z^4y^0 : 1.1e-2$	$z^5y^0 : 2.4e-2$	$z^6y^0 : 9.2e-3$
m=1	$z^0y^1 : -62$	$z^1y^1 : 104$	$z^2y^1 : -8.3$	$z^3y^1 : -1.7$	$z^4y^1 : -4.6e-2$	$z^5y^1 : -1.8e-3$	
m=2	$z^0y^2 : 164$	$z^1y^2 : -13.3$	$z^2y^2 : -0.53$	$z^3y^2 : -0.12$	$z^4y^2 : 0.11$		
m=3	$z^0y^3 : 3.9$	$z^1y^3 : 6.5$	$z^2y^3 : 4.4e-2$	$z^3y^3 : -2.3e-2$			
m=4	$z^0y^4 : 0.95$	$z^1y^4 : 0.21$	$z^2y^4 : -1.9e-2$				
m=5	$z^0y^5 : -3.9e-3$	$z^1y^5 : -6.6e-2$					
m=6	$z^0y^6 : 9.2e-3$						

^aThe calculated polynomial coefficients composing the z-y plane (2D imaging plane) of the Halbach spatial encoding field are shown. Measured points from the linear array of field probes (Fig. 3) were used for this sixth order polynomial fit.

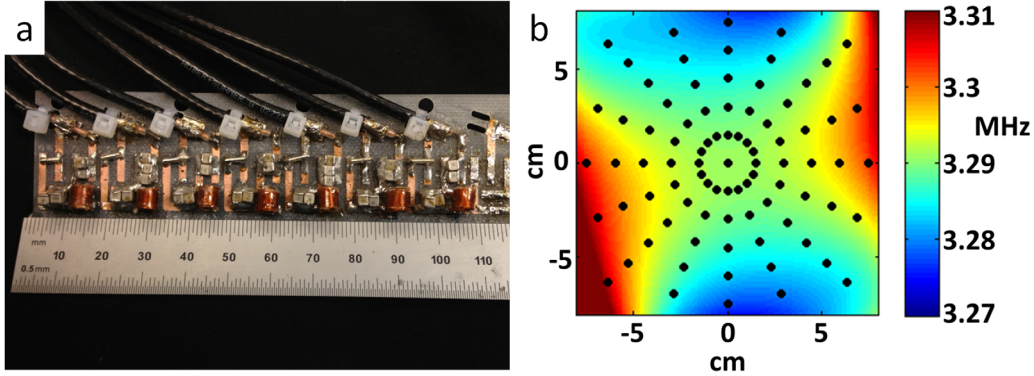


FIG. 3. **a:** Linear array of seven NMR field probes used for mapping the static magnetic field. The probes are held stationary, while the magnet is rotated around them and points on the 2D center plane are sampled. **b:** Measured field map for the center transverse slice through the magnet after fitting 6th order polynomials to the probe data. The black dots mark the location of the probe measurements. The field is plotted in MHz (proton Larmor frequency). This field distribution serves as the SEM information used in image reconstruction.

rotated. The rotating coordinate system of the magnet and the spins is defined as x' , y' , z' (examples shown in Fig. 6b), and the fixed coordinate system for the coils and objects is defined as x , y , z (shown in Figs. 1,2). Image reconstruction requires accurate knowledge of the coil sensitivity map, $C_{q,r}(x)$. Here the index q refers to the coil channel and r to the rotation position of the magnet. The coil sensitivity map is different for each rotation position because B_1^- is formed from a projection of the coil's B_1 field onto the x' - y' plane (which rotates with the magnet). In conventional MRI, B_1^- is mapped by imaging a phantom with fully sampled encoding by the gradient waveforms. However, this approach is not possible with our encoding scheme because knowledge of $C_{q,r}(x)$ is necessary to form an image without aliasing.

Because of the difficulty of measuring B_1^- on our scanner, we use estimated B_1^- maps. Magnetostatic approximations are suitable at the 3.29 MHz Larmor frequency, so B_1 of the individual coils was modeled with Biot-Savart calculations. By symmetry, the x component of the circular surface coils' B_1 is zero in the center plane FOV. The x' component of B_0 is also nearly zero because of the geometry of the magnet. So the coil sensitivity calculation reduces to a two dimensional problem,

because only the B_1 component perpendicular to B_0 contributes to the sensitivity map.

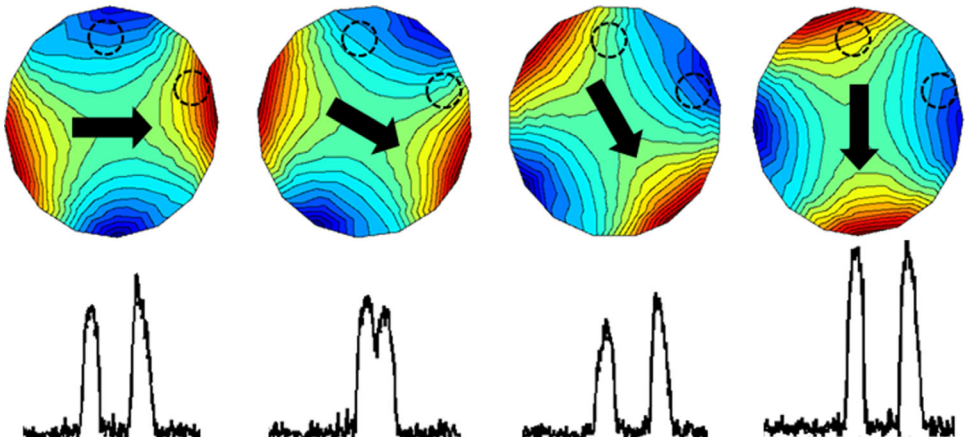
To calculate the coil sensitivity map for each rotation (r), the B_1 component parallel to B_{0r} (the B_0 vector for rotation r) is subtracted and we are left with the perpendicular component.

$$B_{1r}^\perp = B_1 - (B_1 \cdot B_{0r})B_{0r}. \quad [1]$$

The phase is equal to the angle, θ_r , between B_{1r}^\perp and B_{0r} , which will either be $+90^\circ$ or -90° due to the symmetry properties discussed above. The variation in a single coil's B_1^- as a function of B_0 angle is illustrated in Figure 6a,b, and the B_1^- magnitude for four coils and a single B_0 angle is shown in Figure 6c. When B_0 points along the normal to the coil, the sensitivity profile resembles a "donut" pattern with low sensitivity in the center of the FOV. Maximum signal sensitivity occurs when B_0 is oriented orthogonal to the normal vector of the coil loop.

Similar to single-sided imaging methods (7), echo formation requires the use of spin echo sequences in the presence of the inhomogeneous field. The T_2^* of the signal is short due to the static SEM and it is impossible to do the equivalent of gradient echo refocusing because the sign of the SEMs cannot be quickly switched. However,

FIG. 4. Schematic depiction of the generalized projections (bottom row) of an object onto the rotating SEM field. The object consists of two water-filled spheres depicted as dashed black lines which are superimposed on the Halbach magnet's SEM field at a few rotations (black arrow depicts B_0 orientation). The NMR spectrum was acquired with a single volume Rx coil.



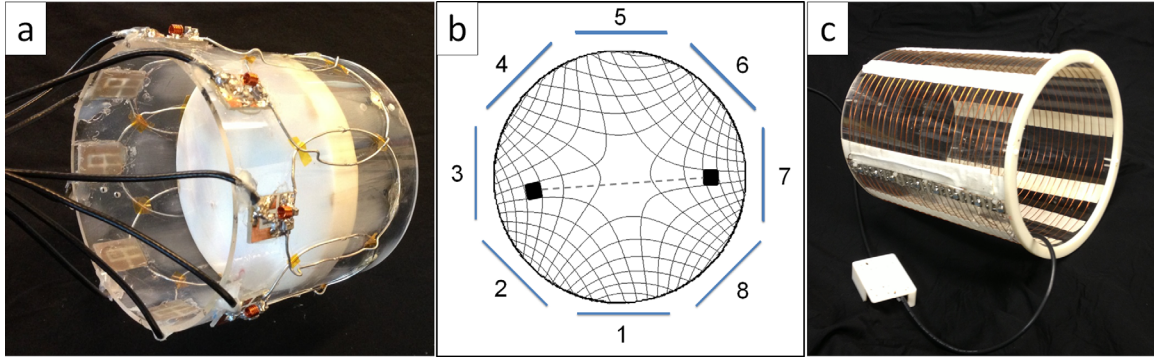


FIG. 5. **a:** Photo of the eight-channel receiver array coil with 3D printed disk-phantom at isocenter. The 14-cm-diameter array is made up of eight, 8-cm loops overlapped to reduce mutual inductance. **b:** Relative voxel size is illustrated as a function of radius from the center using two rotations of the magnet's SEM (field isocontour lines illustrated in figure). Symmetry of the isocontours causes aliasing of each voxel through the origin. Using the local sensitivity profiles of an encircling array of coils, the correct location of each signal source in the FOV can be resolved. (adapted from (28)) **(c)** Photo of the 25 turn, 20-cm diameter, 25-cm length solenoid transmit coil.

the encoding can be repeated and averaged to improve SNR in a spin-echo train, which does refocus the SEM. Unlike in high-field systems, the specific absorption rate (SAR) from the consecutive 180° pulses is negligible because of the low excitation frequency (3.29 MHz).

Unlike conventional MRI scanners, the B_0 field of the Halbach magnet is oriented radially instead of along the

bore of the magnet. This means that in order for B_1^+ to be orthogonal to B_0 at all rotations, it should be directed along the cylindrical axis of the Halbach magnet. This makes a solenoid more suitable than a birdcage coil for radiofrequency (RF) excitation. The constructed solenoid, shown in Figure 5c, has a 20-cm diameter and a 25-cm length. $N = 25$ turns of AWG 20 was chosen as a

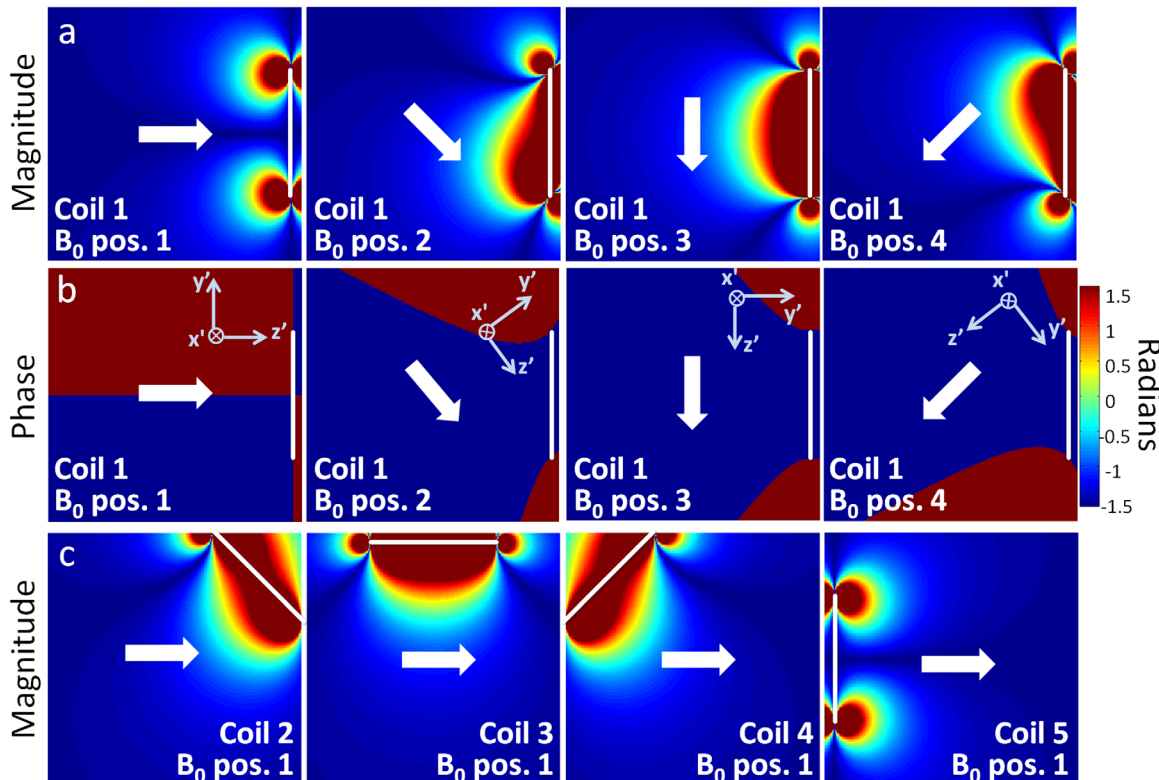


FIG. 6. Biot-Savart calculation of the sensitivity map of the Rx coil array. The white arrows show representative orientations of B_0 , which define the spin coordinate system orientation (x' , y' , z'). Image reconstruction requires accurate coil sensitivity profiles for each B_0 angle used in the experiment. **a,b:** B_1^- magnitude and phase for a single representative surface coil located at the right side of the FOV (position marked with white line). Because of the symmetry of the coils' at isocenter, the coils' x' component is approximately zero, and the process of taking the projection onto the $x'-y'$ plane (to solve for B_1^-) will produce a vector parallel or antiparallel to y' . Therefore, the B_1^- phase is always $+90^\circ$ or -90° in the depicted transverse isocenter plane. **c:** B_1^- magnitude of four different coils of the array (marked with white lines) for a single magnet rotation position.

reasonable value in the tradeoff between B_1^+ homogeneity and parasitic capacitance from closely spaced windings. The 70 uH Tx coil is tuned to 3.29 MHz with eight 230 pF series capacitors distributed along the length of the solenoid, which reduces the susceptibility to stray capacitance. Because the static SEM field is “always on”, the transmit coil must have a relatively low Q to excite a wide bandwidth of spins. The Q of the coil is approximately 60 corresponding to a 55 KHz bandwidth. A 1 KW power amplifier (Tomco, Stepney, SA, Australia) is used to produce short 600 W pulses for broadband excitation (25 μ s for 90° pulses and 50 μ s for 180° pulses).

PIN diode detuning is used in the transmit and receiver coils to prevent coil interaction (25). The tuning/matching circuits are constructed so that the transmit coil is tuned and the receive coils are detuned when the pin diodes are forward biased with console controlled DC voltage. The converse is true when the diodes are reverse biased (Tx coil detuned and Rx coils tuned).

Reconstruction Method

The Halbach magnet’s spatial encoding field is approximately quadrupolar and, therefore, produces a nonbijective mapping between object space and encoding space. This encoding ambiguity leads to aliasing in the image through the origin. As described by Hennig et al (13), parallel imaging with encircling receive coils can be used to disambiguate the nonbijective mapping. This is possible because the coil sensitivity profiles provide additional spatial encoding that localizes signal within each source quadrant of the FOV, eliminating aliasing. This idea is illustrated in Figure 5b. This specific implementation of the portable scanner closely resembles the case of PatLoc imaging with quadrupolar fields and a radial frequency-domain trajectory (28). However, the measured Halbach SEM is not purely quadrupolar, and the presence of arbitrary field components prevents the decomposition of the rotating SEM into linear combinations of two orthogonal encoding fields. For this reason, the direct back-projection reconstruction method described in Schultz et al (28) is not valid, and iterative matrix methods such as those described in Stockmann et al (29) are used.

The discretized signal acquired by a coil (q) at a given magnet rotation (r) at time n can be described as

$$s_{q,r}(n) = \sum_{\mathbf{x}} C_{q,r}(\mathbf{x}) e^{-i2\pi k(r,\mathbf{x},n)} m(\mathbf{x}) \quad [2]$$

where $m(\mathbf{x})$ is the magnetization of the object at location vector \mathbf{x} , $C_{q,r}(\mathbf{x})$ is the complex sensitivity of the coil at location \mathbf{x} , and $k(r,\mathbf{x},n)$ is the evolved phase from the nonlinear gradient at rotation r , location \mathbf{x} , and time n . The exponential term and coil sensitivity term can be grouped together to form the encoding function $enc_{q,r}(\mathbf{x}, n)$.

$$s_{q,r}(n) = \sum_{\mathbf{x}} enc_{q,r}(\mathbf{x}, n) m(\mathbf{x}) \quad [3]$$

The matrix form of this signal equation for a single projection readout acquired with one RF coil is simply

$$\mathbf{S}_{q,r} = \mathbf{E}_{q,r} \mathbf{m}. \quad [4]$$

The acquired signal, $\mathbf{S}_{q,r}$, is a vector made up of the sampled readout points (N_{smp}). The object that we are solving for, \mathbf{m} , is a vector made up of all the image voxels (N_{vox}). The encoding matrix, $\mathbf{E}_{q,r}$, contains the evolved phase of each voxel in the FOV for each time point in the acquisition as well as the coil sensitivity multiplier. With linear gradient fields, \mathbf{E} is made up of the sinusoidal Fourier basis set, which allows the image to be reconstructed using radial back-projection, k-space re-gridding, and other approaches. In the nonlinear SEM case, \mathbf{E} is more complicated, but can be calculated from the measured field maps. Before the appropriately rotated field map is used to calculate the phase evolution, the field change captured by the navigator probe during the acquisition is added as a global offset.

A separate block of the encoding matrix, $\mathbf{E}_{q,r}$ is calculated for the data acquired by each coil at each rotation. There will be a total of $R*C$ blocks (where R is total number of rotation and C is the total number of coils), which are vertically concatenated to form the full encoding matrix, \mathbf{E} . \mathbf{S} is also made up of vertically concatenated subparts, $\mathbf{S}_{q,r}$, which are the signals acquired from each coil at each rotation.

To reconstruct the image from the acquired data, the object, \mathbf{m} , can be found by inverting the matrix, \mathbf{E} . However, the full encoding matrix size is $N_{smp} * R * C \times N_{vox}$. In the typical case of 256 readout points, 181 rotations, eight coils, and a 256 × 256 voxel reconstructed image, the full matrix size is 371K × 65K. Because it is not computationally feasible to invert this matrix, iterative methods such as the Conjugate Gradient method (30) and the Algebraic Reconstruction Technique (31,32) can be used to solve for the minimum norm least squares estimator of \mathbf{m} . The generality of this approach allows arbitrary field shapes and coil profiles as well as systematic errors such as temperature-dependent field drifts to be incorporated into the encoding matrix.

The reconstructed images and simulations shown here were done using the Algebraic Reconstruction Technique. The encoding matrix was calculated line by line during the reconstruction using the appropriately rotated and temperature drift-corrected field map and the calculated coil sensitivity profiles for the given B_0 direction. To demonstrate the importance of temperature drift compensation, a phantom image was also reconstructed with an uncorrected encoding matrix. The field of view of the images is 16 cm and the in-plane voxel size is 0.625 mm.

Phantom Imaging Methods

Images of a “MIT/MGH” phantom were acquired both with a single channel solenoid Rx coil and with seven coils of the Rx array. The 3D printed polycarbonate phantom is 1.7-cm thick with a 13-cm diameter, and is filled with CuSO₄-doped water. Thirty-two averages of a six spin-echo train (TR = 550 ms, echo-spacing = 8ms) were acquired for 91 rotation angles over 180 degrees. Navigator field probe data was also acquired at each rotation. The coil array’s lengthy acquisition time of 66 min

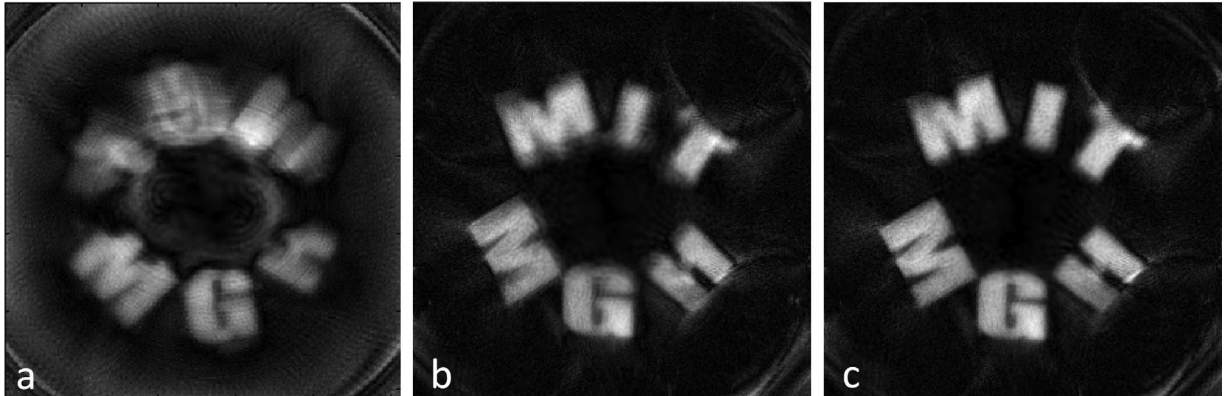


FIG. 7. Experimental 256×256 voxel, 16-cm FOV images of a 3D printed phantom with CuSO_4 doped water occupying the interior of the letters and polycarbonate plastic surrounding it. The phantom has a 13-cm diameter and is 1.7 cm thick. 91 magnet rotations spaced 2° apart were used, readout bandwidth/Npts = 40 KHz/256, TR = 550 ms, spin-echo train length = 6 or 16, with 8 ms echo-spacing. Echoes in the spin-echo train for a given rotation were averaged. **a:** Image acquired with solenoid Rx coil (32 averages of a 6 spin-echo train). **b:** Image acquired with seven coils of the Rx coil array (8 averages of a 16 spin-echo train). Temperature drift was not corrected for. **c:** Image from same data as (B), but with temperature drift correction implemented.

results from multiplexing a single console receiver and would be reduced to 7.3 min by acquiring data from all channels and the field probe in parallel.

A 1-cm-thick lemon slice was imaged using only the bottom five surface coils with 181 1° rotations. The total acquisition time was 93 minutes (15.5 min if surface coils and navigator probe were acquired in parallel). A single average of a 128 echo train at each rotation provided sufficient SNR. Each echo was recorded as 256 pts with a 40 KHz BW (TR = 4500 ms, echo spacing = 8 ms). For comparison, the lemon image was also reconstructed using only 91 rotations of 181 acquired rotations in addition to the full reconstruction.

Image Simulation Methods

The described acquisition method was simulated using the measured field map from the central slice of the Halbach magnet. Images were simulated using a high resolution T_1 brain image or a numerically generated checkerboard with 2.5-mm grid size as the “object.” The measured field map and calculated coil profiles of the eight coil array were used in the forward model to generate the simulated data. In one simulation, an artificial field map was used to simulate the addition of a linear field component to measured SEM. Complex noise was added to the simulations to match noise levels observed in comparable phantom projection. These simulations were done with the same sequence parameters of the lemon image: 181 1° magnet rotations, 256 pt readout, 40 KHz BW, echo spacing = 8 ms.

RESULTS

Experimental images of the 3D printed “MIT/MGH” phantom are shown in Figure 7. The image acquired with the solenoid coil used in transmit/receive mode is shown in Figure 7a. Only the “MGH” part of the phantom was filled at the time, so the top half of the image should ideally be empty. Instead the expected aliasing pattern is seen through the center onto frequency

matched quadrants of the FOV. The aliased image is markedly more blurry than one would expect for a purely quadrupolar field, which maps all signals symmetrically about the center during reconstruction. This discrepancy likely arises due to the presence of first-order and higher-order field terms which perturb the symmetry of the dominant quadrupolar field.

The importance of monitoring and correcting for field drift due to temperature is emphasized by comparing Figure 7b and Figure 7c which show images with and without temperature drift correction. The drift correction is achieved by monitoring the frequency seen by the navigator field probe which rotates with the magnet. This probe’s frequency is ideally independent of the rotation angle during the acquisition, but varies due to two causes. First, small changes in room temperature translate to a global scaling of the Halbach array’s magnetization and thus the central B_o . With no attempt to insulate or stabilize the magnet’s temperature, changes up to 0.4 $^\circ\text{C}$ and 1.6 KHz were observed over an hour. The second cause for the fixed probe’s change in field as a function of rotation is due to the changing vector sum of the earth’s field and the Halbach field. This effect creates a peak-peak variation of 3.7 kHz for the magnet location and orientation. This effect must also be incorporated in the encoding matrix. Even though field drift correction is applied to Figure 7c, some of the letters are sharper than others; this is likely attributable to field map inaccuracies.

The 1-cm lemon slice images are seen in Figure 8. The use of five of eight coils of the receive array prevents aliasing in the image, but center blurring is more pronounced in these images than in the simulations (Fig. 9). Figure 8a was reconstructed using half of the rotations angles of Figure 8b, resulting in poorer image quality and streaking artifacts.

Figure 9 shows an encoding and reconstruction simulation using a typical high field T_1 -weighted brain MRI as the imaging object (Fig. 9a). Noise was added to the object model to simulate the lower SNR of the low field

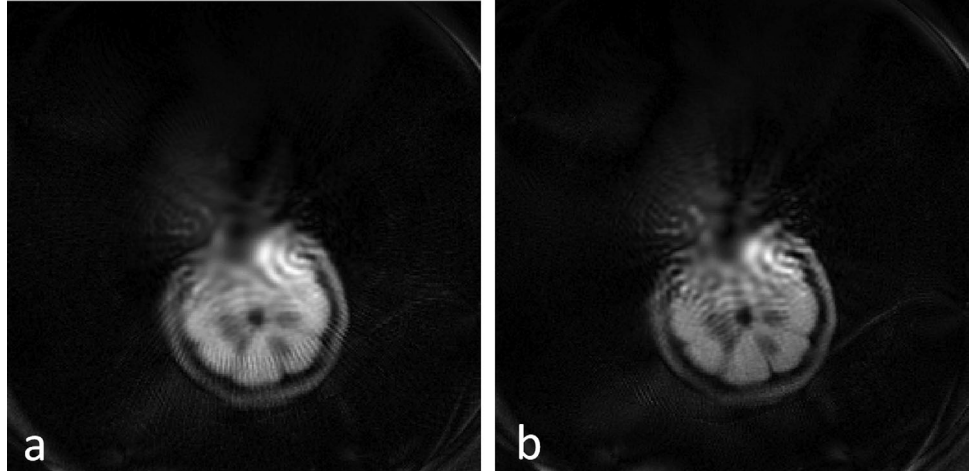


FIG. 8. Experimental 256×256 voxel, 16-cm FOV image of a 1-cm thick slice of lemon placed off axis in the magnet. Five receiver coils of the array were used to acquire one average of a 128 spin-echo train, readout bandwidth/Npts = 40 KHz/256, TR = 4500 ms, echo-spacing = 8 ms. **a:** 91 magnet rotations spaced 2° apart were used (**b**) 181 magnet rotations spaced 1° apart were used.

scanner. Figure 9b shows a simulated image using the measured encoding field of Halbach magnet. There is no aliasing in the image because the calculated coil sensitivity profiles of the eight channel Rx array were used. However, there is blurring in the center which coincides with the shallow region of the nonlinear gradient field. The center blurring in Figure 9c is reduced because the image was simulated using an artificial field map that consists of our measured SEM plus an additional linear field of 500 Hz/cm. The simulation of the 2.5-mm grid numerical phantom (Fig. 9d) shows the ultimate resolution possible with the existing experimental protocol in the absence of systematic errors. Outstanding resolution at the periphery gradually gives way to a blurry central region.

DISCUSSION

As expected, the nonbijective mapping of the Halbach magnet's SEM results in aliasing. Fortunately, as

described in Hennig et al (13) the aliasing is resolved by the addition of a multichannel receive array with differing spatial profiles and an appropriate geometry. Because the Halbach encoding is dominated by the quadrupolar "PatLoc" SEM, the system's spatially varying voxel size changes approximately as c/ρ within the FOV, where ρ is the radius and the constant c depends on the strength of the SEM and the length of the readout (27). This means that our Halbach magnet encoding field results in higher resolution at the periphery due to the uniform nature of the SEM near the center of the FOV. This center blurring is seen in both the experimental images in Figure 8 and the simulations in Figure 9.

While we did not attempt to control the precise spherical harmonic distribution in the magnet design, future work will likely benefit from shimming the magnet to obtain a more desirable SEM. For example, if a sufficient linear term were added, the uniform encoding field region would not lie on-axis with the rotation. In this case,

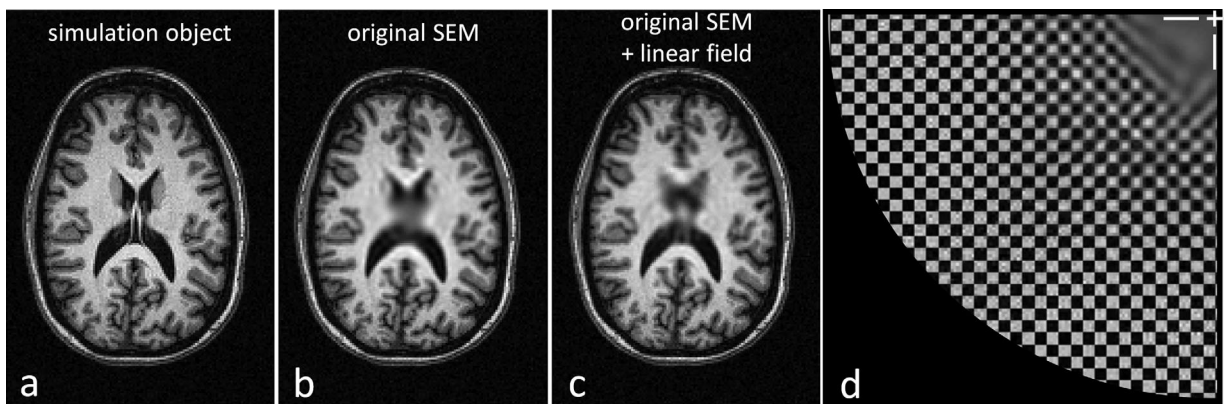


FIG. 9. Simulated images using the calculated sensitivity profiles of the eight coil Rx array to generate the forward model for 181 1° rotations of the encoding field, 6.4 ms, 256 point readouts. The data seen by the Halbach scanner was simulated by processing this "object" through the forward model and adding noise to make it consistent with the SNR of the time-domain signals measured in a water phantom. The model data was then reconstructed using the Algebraic Reconstruction Technique in a 16-cm FOV. **a:** Reference high resolution 3T T₁ weighted brain image used as the model object. Note: the SEMs were scaled to the brain FOV. **b:** Simulated reconstruction using the measured SEM to generate the forward model. **c:** Simulated reconstruction using the measured SEM with the additional artificial linear field component (500 Hz/cm). **d:** Simulated reconstruction of a 2.5-mm grid numerical phantom. Only one quadrant of the FOV is shown, the center of the FOV is marked with white cross-hairs in the upper right.

which is simulated in Figure 9c, the “blind-spot” would move around the object allowing some rotations to contribute to encoding of any given pixel, as previously explored in “O-space imaging” (14). Pursuing this strategy even further would result in a SEM containing only a linear term. In this case, the encoding becomes very similar to a radial imaging scheme with conventional gradients, and to the strategy proposed by Cho et al. who used a rotating gradient coil in a conventional magnet (12). With accurate field mapping instrumentation and shimming software, we suspect that the magnet could be shimmed to a more desirable SEM. Although a linear SEM would eliminate the encoding hole and allow a more straightforward reconstruction method, there are advantages to second-order SEMs, including the coincidence of the high spatial resolution area and high coil sensitivity area near the edge of the FOV.

The lemon images of Figure 8 show that when 91 projection rotations are used instead of 181, a radial streaking artifact is visible. The streaking artifacts are consistent with those arising in conventional undersampled radial trajectories played by linear SEMs as well as undersampled radial trajectories played by PatLoc SEMs (27). It has been shown that the use of total variation and total generalized variation priors during reconstruction suppresses streaking artifacts in undersampled conventional radial (33) and PatLoc radial (34) acquisitions. Similar techniques may be pursued in future work to suppress streaking in images obtained with fewer projection rotations of our scanner.

The simulations in Figure 9 show the theoretical resolution of the scanner when systematic errors are eliminated. These errors are most likely a result of field map and coil sensitivity profile inaccuracies, which are critical to the iterative reconstruction (14). The current coil sensitivity profiles facilitate proof-of-concept reconstructions, but their fidelity is suspect because they were calculated rather than measured. In these calculations the magnetostatic Biot Savart approximation was used with no external structures present. While wavelength effects in the body are not expected at this frequency, the close proximity of the conducting magnets and other coils might perturb the experimental fields. Additionally, a 2D field map is currently used to reconstruct thin samples (1 to 1.5 cm thick), but field variation does exist in the x direction (along the axis of the Halbach cylinder) within the sample thickness. This causes through-plane dephasing and must be incorporated into the encoding matrix based on a 3D field map.

Field map errors arise from temperature drifts which are significant on the time scale of the imaging and mapping acquisitions. We have shown that any uncorrected temperature drift causes substantial blurring in the image (Fig. 7b). Temperature drift is a pervasive problem in permanent magnet MRI and has been addressed in several ways. In the current experimental protocol the frequency at a fixed point is measured at every rotation and the drift is built into the encoding matrix as a global offset to the field maps. This method reduces blurring considerably (Fig. 7c), but other options have been proposed for permanent magnet NMR and MRI that may offer

higher encoding matrix accuracy. For example, Kose and Haishi (1) describe the implementation of a NMR lock method plus thermal insulation. Additionally, a new Halbach design was recently reported which uses two types of magnet materials with different temperature coefficients to substantially reduce the effect of temperature changes on the B_0 field (35). When compared with an uncompensated SmCo magnet, this reduced their temperature coefficient 100-fold, bringing the field drift down to 10 ppm for a 3°C temperature change. However this method has the disadvantage of producing a lower field and requiring more magnet material than the traditional design.

For time-efficient acquisitions, true parallel imaging will be needed. To accomplish this goal, a multichannel receiver console is required, as well as the implementation of preamp decoupling. This is advantageous for practical diagnostic reasons and will also alleviate the field drift problem by shortening acquisition times. In addition to multiple channels, future prototypes must be made larger to accommodate the human head. Although the head can be fit into the presented magnet, its 36-cm diameter does not leave sufficient room for the transmit and receive arrays as well as the structural supports for the magnetic material. Construction of a larger diameter magnet with the same basic design will result in a reduced B_0 field, although this could be mitigated by adding more magnet material and/or higher grade material. The current B_0 field of 77.3 mT is estimated to decrease to 62 mT if the diameter is increased to 40 cm. However if 24 N45 NdFeB magnet rungs are used instead of 20 N42 rungs, a field of 80 mT is theoretically achievable. The standard landmark for brain imaging (between the eyebrows) is 18 cm above the shoulders. The presented Halbach magnet was designed using the maximum cylinder length that allows the brain to be centered in the magnet (2 × 18 cm). Future magnet designs will likely adhere to this constraint because increasing the length of the magnet requires increasing the bore size to fit shoulders, which would result in a considerably weaker B_0 .

In the described experiments the B_0 field rotates relative to the receiver coils (coils are stationary), which causes the shape of the coil profiles to change with each acquisition angle. However this arrangement is not a requirement for rotating SEM imaging, and in theory the receiver coils could rotate with the magnet. In this case, the coil sensitivity profiles are simply rotated for each acquisition angle, but the shapes of profiles do not change. Data acquisition with rotating coils and stationary coils was simulated. However, there was not a significant difference in performance in either the visual appearance of the reconstructed images or the RMSE (root mean squared error). For data simulated with 91 magnet rotations there was a 0.2% RMSE improvement when using the rotating coil profiles, and for data simulated with 23 magnet rotations (undersampled) there was a 3.6% RMSE improvement. This suggests that rotating the coil array may improve performance when data is undersampled. The 23 rotation simulated images are included in the supplemental material. The rotating receive coil case is similar to the RRFC (Rotating RF

Coils) method described in Trakic et al and Li et al (36,37), where continuously rotating surface coils are used in a conventional magnet for parallel imaging.

The goal of the current work was to provide a proof-of-principle that the basic 2D encoding scheme can be performed, which was demonstrated with 2D imaging of thin samples. However, the addition of third axis encoding is an obvious requirement for medical applications. A promising possibility for encoding the third dimension (along the axis of rotation) is TRASE (15,16). TRASE uses custom-designed RF coils to generate uniform amplitude but linear B_1^+ phase variation along the encoding axis. Spatial encoding is achieved using at least two Tx coils with different phase gradients (typically differing by their sign). Spin-echo trains are used in which the linear phase variation is changed by 180 degrees in between successive refocusing pulses. As the sign of the refocusing pulse is flipped over the course of the echo train, k-space is traversed one echo at a time. The resolution depends on the number of echoes used and the slope of the transmitted B_1 phase ramp across the FOV (16). The approach is synergistic with the echo trains used in the presented encoding scheme for purposes of signal averaging. Furthermore, at low field, TRASE spin-echo trains do not suffer from the SAR limits that may impact the method's performance at high field.

CONCLUSIONS

Using an inhomogeneous magnet for spatial encoding in lieu of gradient coils, we have constructed and demonstrated a lightweight scanner for 2D MR imaging with minimal power requirements. The 2D proof-of-concept images from this nearly head-sized imager show the ability of this encoding scheme to produce sufficient spatial resolution and sensitivity for the detection and characterization of many common neurological disorders such as hydrocephalus and traumatic space-occupying hemorrhages. Future work in perfecting the calibration methods is likely to bring experimental image quality closer to the theoretical limit, but the resolution of the current system is sufficient for identifying gross pathologies. With the future implementation of true parallel imaging and 3D encoding, this scanner has the potential to enable a truly portable, low-cost brain imaging device.

ACKNOWLEDGMENTS

The authors thank Matthew Christensen and Cris LaPierre for their 3D modeling and design work, Bastien Guerin for advice on calculating coil sensitivities, and Stephen Cauley for help with reconstruction methods. This research was carried out at the Athinoula A. Martinos Center for Biomedical Imaging at the Massachusetts General Hospital, using resources provided by the Center for Functional Neuroimaging Technologies. This project was supported by a training grant from the NIH Blueprint for Neuroscience Research. Its contents are solely the responsibility of the authors and do not necessarily represent the official views of the NIH.

REFERENCES

- Kose K, Haishi T. High resolution NMR imaging using a high field yokeless permanent magnet. *Magn Reson Med Sci* 2011;10:159–167.
- Kimura T, Geya Y, Terada Y, Kose K, Haishi T, Gemma H, Sekozawa Y. Development of a mobile magnetic resonance imaging system for outdoor tree measurements. *Rev Sci Instrum* 2011;82:053704.
- Gerlach R, du Mesnil de Rochemont R, Gasser T, Marquardt G, Reusch J, Imoehl L, Seifert V. Feasibility of Polestar N20, an ultra-low-field intraoperative magnetic resonance imaging system in resection control of pituitary macroadenomas: lessons learned from the first 40 cases. *Neurosurgery* 2008;63:272–284; discussion 284–285.
- Jackson JA, Burnett LJ, Harmon JF. Remote (inside-out) NMR. III. Detection of nuclear magnetic resonance in a remotely produced region of homogeneous magnetic field. *J Magn Reson* 1980;41:411–421.
- Sagawa M, Fujimura S, Togawa N, Yamamoto H, Matsuura Y. New material for permanent magnets on a base of Nd and Fe (invited). *J Appl Phys* 1984;55:2083–2087.
- Kleinberg R, Sezginer A, Griffin D, Fukuhara M. Novel NMR apparatus for investigating an external sample. *J Magn Reson* 1992;97:466–485.
- Casanova F, Perlo J, Blümich B. Single-sided NMR. New York: Springer; 2011.
- Eidmann RS. The NMR MOUSE, a mobile universal surface explorer. *J Magn Reson Series A* 1996;122:104–109.
- Todica M, Fechete R, Blümich B. Selective NMR excitation in strongly inhomogeneous magnetic fields. *J Magn Reson* 2003;164: 220–227.
- Perlo J, Casanova F, Blümich B. 3D imaging with a single-sided sensor: an open tomograph. *J Magn Reson* 2004;166:228–235.
- Landeghem MV, Danieli E, Perlo J, Blümich B, Casanova F. Low-gradient single-sided NMR sensor for one-shot profiling of human skin. *J Magn Reson* 2012;215:74–84.
- Cho ZH, Chung ST, Chung JY, Park SH, Kim JS, Moon CH, Hong IK. A new silent magnetic resonance imaging using a rotating DC gradient. *Magn Reson Med* 1998;39:317–321.
- Hennig J, Welz AM, Schultz G, Korvink J, Liu Z, Speck O, Zaitsev M. Parallel imaging in non-bijective, curvilinear magnetic field gradients: a concept study. *Magn Reson Mater Phys* 2008;21:5–14.
- Stockmann JP, Galiana G, Tam L, Juchem C, Nixon TW, Constable RT. In vivo O-Space imaging with a dedicated 12 cm Z2 insert coil on a human 3T scanner using phase map calibration. *Magn Reson Med* 2013;69:444–455.
- Sharp JC, King SB. MRI using radiofrequency magnetic field phase gradients. *Magn Reson Med* 2010;63:151–161.
- Sharp JC, King SB, Deng Q, Volotovskyy V, Tomanek B. High-resolution MRI encoding using radiofrequency phase gradients. *NMR Biomed* 2013;26:1602–1607.
- Zimmerman C, Blau J, Rosen MS, Wald LL. Design and construction of a Halbach array magnet for portable brain MRI. In Proceedings of the 20th Annual Meeting of ISMRM, Melbourne, Australia, 2012. Abstract 2575.
- Cooley CZ, Stockmann JP, Armstrong BD, Rosen MS, Wald LL. A lightweight, portable MRI brain scanner based on a rotating Halbach magnet. In Proceedings of the 21st Annual Meeting of ISMRM, Salt Lake City, Utah, USA, 2013. Abstract 137.
- Stockmann JP, Cooley CZ, Rosen MS, Wald LL. Flexible spatial encoding strategies using rotating multipolar fields for unconventional MRI applications. In Proceedings of the 21st Annual Meeting of ISMRM, Salt Lake City, Utah, USA, 2013. Abstract 2664.
- Raich H, Blümler P. Design and construction of a dipolar Halbach array with a homogeneous field from identical bar magnets: NMR Mandhalas. *Concepts Magn Reson Part B Magn Reson Eng* 2004;23B: 16–25.
- Wroblewski P, Szyszko J, Smolik WT. Mandhala magnet for ultra low-field MRI. In 2011 IEEE International Conference on Imaging Systems and Techniques (IST), 2011. pp. 248–252.
- Halbach K. Design of permanent multipole magnets with oriented rare earth cobalt material. *Nucl Instrum Methods* 1980;169:1–10.
- De Zanche N, Barmet C, Nordmeyer-Massner JA, Pruessmann KP. NMR probes for measuring magnetic fields and field dynamics in MR systems. *Magn Reson Med* 2008;60:176–186.

24. Schultz G, Gallichan D, Reisert M, Hennig J, Zaitsev M. MR image reconstruction from generalized projections. *Magn Reson Med* 2013; doi: 10.1002/mrm.24928.
25. Edelstein W, Hardy C, Mueller O. Electronic decoupling of surface-coil receivers for NMR imaging and spectroscopy. *J Magn Reson* (1969). 1986;67:156–161.
26. Roemer PB, Edelstein WA, Hayes CE, Souza SP, Mueller OM. The NMR phased array. *Magn Reson Med* 1990;16:192–225.
27. Schultz G, Ullmann P, Lehr H, Welz AM, Hennig J, Zaitsev M. Reconstruction of MRI data encoded with arbitrarily shaped, curvilinear, nonbijective magnetic fields. *Magn Reson Med* 2010;64:1390–1403.
28. Schultz G, Weber H, Gallichan D, Witschey WRT, Welz AM, Cocosco CA, Hennig J, Zaitsev M. Radial imaging with multipolar magnetic encoding fields. *IEEE Trans Med Imaging* 2011;30:2134–2145.
29. Stockmann JP, Ciris PA, Galiana G, Tam L, Constable RT. O-space imaging: highly efficient parallel imaging using second-order nonlinear fields as encoding gradients with no phase encoding. *Magn Reson Med* 2010;64:447–456.
30. Hestenes M, Stiefel E. Methods of conjugate gradients for solving linear systems. *J Res Natl Bur Stand* 1952;49:409–436.
31. Kaczmarz S. Angenäherte Auflösung von Systemen linearer Gleichungen. *Bull Int Acad Pol Sci let Cl Med.* 1937;35:355–357.
32. Gordon R, Bender R, Herman GT. Algebraic reconstruction techniques (ART) for three-dimensional electron microscopy and x-ray photography. *J Theor Biol* 1970;29:471–481.
33. Block KT, Uecker M, Frahm J. Undersampled radial MRI with multiple coils. Iterative image reconstruction using a total variation constraint. *Magn Reson Med* 2007;57:1086–1098.
34. Knoll F, Schultz G, Bredies K, Gallichan D, Zaitsev M, Hennig J, Stollberger R. Reconstruction of undersampled radial PatLoc imaging using total generalized variation. *Magn Reson Med* 2013;70:40–52.
35. Danieli E, Perlo J, Blümich B, Casanova F. Highly stable and finely tuned magnetic fields generated by permanent magnet assemblies. *Phys Rev Lett* 2013;110:180801.
36. Trakic A, Weber E, Li BK, Wang H, Liu F, Engstrom C, Crozier S. Electromechanical design and construction of a rotating radiofrequency coil system for applications in magnetic resonance. *IEEE Trans Biomed Eng* 2012;59:1068–1075.
37. Li M, Jin J, Trakic A, Liu F, Weber E, Li Y, Crozier S. High acceleration with a rotating radiofrequency coil array (RRFCA) in parallel magnetic resonance imaging (MRI). In 2012 Annual International Conference of the IEEE Engineering in Medicine and Biology Society (EMBC), 2012. p 1098–1101.